

COMPARATIVE STUDY ON SURFACE ENHANCED RAMAN SCATTERING
ACTIVITY OF VARIOUS SILVER NANOSTRUCTURES

A THESIS SUBMITTED TO
THE GRADUATE SCHOOL OF NATURAL AND APPLIED SCIENCES
OF
MIDDLE EAST TECHNICAL UNIVERSITY

BY

ÖZGE DEMİRTAŞ

IN PARTIAL FULFILLMENT OF THE REQUIREMENTS
FOR
THE DEGREE OF MASTER OF SCIENCE
IN
PHYSICS

JANUARY 2017

Approval of the thesis:

**COMPARATIVE STUDY ON SURFACE ENHANCED RAMAN
SCATTERING ACTIVITY OF VARIOUS SILVER NANOSTRUCTURES**

submitted by **ÖZGE DEMİRTAŞ** in partial fulfillment of the requirements for the degree of **Master of Science in Physics Department, Middle East Technical University** by,

Prof. Dr. Gülbin Dural Ünver
Dean, Graduate School of **Natural and Applied Sciences**

Prof. Dr. Sadi Turgut
Vice Head of Department, **Physics**

Assoc. Prof. Dr. Alpan Bek
Supervisor, **Physics Dept., METU**

Examining Committee Members:

Prof. Dr. Mehmet Parlak
Physics Dept., METU

Assoc. Prof. Dr. Alpan Bek
Physics Dept., METU

Assoc. Prof. Dr. M. Emre Taşgın
Institute of Nuclear Sciences, Hacettepe University

Assoc. Prof. Dr. Serhat Çakır
Physics Dept., METU

Assoc. Prof. Dr. H. Emrah Ünalın
Metallurgical and Materials Engineering Dept.,
METU

Date: 27.01.2017

I hereby declare that all information in this document has been obtained and presented in accordance with academic rules and ethical conduct. I also declare that, as required by these rules and conduct, I have fully cited and referenced all material and results that are not original to this work.

Name, Last Name: ÖZGE DEMİRTAŞ

Signature:

ABSTRACT

COMPARATIVE STUDY ON SURFACE ENHANCED RAMAN SCATTERING ACTIVITY OF VARIOUS SILVER NANOSTRUCTURES

Demirtaş, Özge

M.S., Department of Physics

Supervisor: Assoc. Prof. Dr. Alpan Bek

Co-Supervisor: Assoc. Prof. Dr. Mehmet Emre Taşgın

January 2017, 75 pages

In this work, the effect of the strong field enhancement generated in the near field of metal nanoparticles and nanowires was investigated by taking advantage of the plasmon frequencies induced by Raman laser light stimulation of free conduction electrons of these metal nanostructures. Small number of molecules that are either bound to these nanostructures or located up to a few nanometers away from the nanostructures can be detected easily through strong electromagnetic field enhancement. The aim of this work was to investigate the surface enhanced Raman scattering (SERS) effect of crystal violet (CV) and brilliant cresyl blue (BCB) molecules interacting with silver nanoparticle (Ag NP) and silver nanowire (Ag NW) that are deposited onto silicon surfaces. Statistical measurements on SERS effect, which is an application of localized surface plasmon resonance (LSPR) were acquired and corresponding enhancement factor (EF) ranges were revealed. The fact that plasmon lifetime of polyol synthesized colloidal Ag NPs and Ag NWs are long due to their smooth crystalline surfaces at the atomic level providing strong plasmon interaction of these structures. In addition, the interaction between nanostructures also depends on the number of hot spots between aggregated nanostructures, and the LSPR wavelength. Although LSPR wavelengths of nanostructures and maximum

absorption wavelength of the analytes used in this work are not in resonance with the laser light, maximum EF values documented in the literature were obtained.

Keywords: Surface enhanced Raman scattering, Colloidal silver nanoparticle, colloidal silver nanowire, Crystal violet, Brilliant cresyl blue.

ÖZ

ÇEŞİTLİ GÜMÜŞ NANOYAPILARIN YÜZEYDE GÜÇLENDİRİLMİŞ RAMAN SAÇILMASI AKTİFLİĞİ ÜZERİNE KARŞILAŞTIRMALI ARAŞTIRMASI

Demirtaş, Özge

Yüksek Lisans, Fizik Bölümü

Tez Yöneticisi: Doç. Dr. Alpan Bek

Ortak Tez Yöneticisi: Doç. Dr. Mehmet Emre Taşgın

Ocak 2017, 75 sayfa

Bu çalışmada, metal nanoparçacık ve nanotellerin serbest iletim elektronlarının lazer ışığıyla uyarılmasıyla meydana gelen plazmon frekanslarından faydalanarak, bu nanoyapıların yakın alanında oluşan kuvvetli alan artırımının etkisi incelenmiştir. Bu nanoyapılara tutunan ya da en fazla bir kaç nanometre kadar uzağına yerleşmiş olan az sayıdaki molekül yüksek elektromanyetik alan artırımını sayesinde kolaylıkla tespit edilebilir. Lokalize olmuş yüzey plazmon rezonansının (LSPR) bir uygulanması olan yüzey artırımı Raman saçılması (YARS) üzerindeki istatistiksel ölçümler alınmış ve bunlara karşılık gelen artırım faktörü (AF) aralıkları gösterilmiştir. Bu çalışmada silikon yüzeyler üzerine kaplanmış gümüş nanoparçacık (Ag NP) ve gümüş nanotellerle (Ag NW) etkileşim halinde olan crystal violet (CV) ve brilliant cresyl blue (BCB) moleküllerinin YARS etkisini incelemek hedeflenmiştir. Polyol yöntemiyle sentezlenmiş Ag NP ve Ag NW yapılarının yüzeylerinin atomik seviyede pürüzsüz kristal yapıda olması sebebiyle plazmon ömürlerinin uzun olması bu yapıların plazmon etkileşimlerini güçlü kılmaktadır. Buna ek olarak, nanoyapılar arasındaki etkileşim aynı zamanda kümelenmiş nanoyapılar arasındaki etkin bölge

sayısına ve LSPR dalga boyuna da baęlıdır. Bu alıřmada kullanılan nanoyapıların LSPR dalgaboyları ve analitlerin maksimum soęurma dalga boyları lazer ışığı ile rezonansta olmamasına raęmen, literatürde belgelenmiř maksimum AF deęerleri elde edilmiřtir.

Anahtar Kelimeler: Yüzey artırımlı Raman saęılması, Asıltılı gümüş nanoparacık, Asıltılı gümüş nanotel, Crystal violet, Brilliant cresyl blue.

To my family

ACKNOWLEDGMENTS

First and foremost, I would like to express my sincerest gratitude to my advisor Assoc. Prof. Dr. Alpan Bek for his guidance and patience. He supported and guided me with his immense knowledge and enthusiasm all the time.

I would like to thank Prof. Dr. Raşit Turan for giving me the opportunity of working in GÜNAM laboratories. I also thank to Assoc. Prof. Dr. Emrah Ünalın, Recep Yüksel and members of METE Nanolab for their help in my studies.

I am thankful to Assoc. Prof. Dr. Mehmet Emre Taşgın and Zafer Artvin for their cooperation and help with simulations.

I would like to thank members of Nano-Optics research group especially to Gizem Birant, Kurtuluş Abak, Tahir Çolakođlu, Murat Öztürk, Mete Günöven, Mona Zolfaghari Borra and Ezgi Aygün that helped and supported me all the time.

I kindly acknowledge financial support from TÜBİTAK under project no: 113F239 and 113M931.

I would like to thank my best friends Cansu Karatay and Fulya Demir keeping me motivated all the time. I also would like to express my endless thanks to Ođuz Can Özyazıcı for encouraging me whenever I need.

Last but not least, I would like to thank my family: my parents and my brother whose love and guidance are with me throughout all my life.

TABLE OF CONTENTS

ABSTRACT.....	v
ÖZ.....	vii
ACKNOWLEDGMENTS.....	x
TABLE OF CONTENTS.....	xi
LIST OF TABLES.....	xiii
LIST OF FIGURES.....	xiv
CHAPTERS	
1 INTRODUCTION.....	1
2 THEORY.....	7
2.1 Raman Scattering.....	7
2.2 Enhancement Mechanism.....	11
2.3 Surface Enhanced Raman Scattering.....	14
2.3.1 Electromagnetic-Field Enhancement.....	14
2.3.1.1 Optical Properties of Noble Metals.....	15
2.3.1.2 Surface Plasmons.....	18
2.3.1.3 Localized Surface Plasmons.....	19
2.3.2 Chemical Field Enhancement.....	24
2.4 Enhancement Factor.....	25
3 EXPERIMENTAL TECHNIQUES.....	29
3.1 Synthesis.....	29
3.1.1 Polyol Synthesis of Ag NPs.....	31
3.1.2 Polyol Synthesis of Ag NWs.....	31
3.2 Substrate Preparation.....	32
3.3 Characterization.....	34

3.3.1 SEM Analysis.....	34
3.3.2 Raman Measurements.....	34
3.3.3 Reflection Measurements.....	35
4 RESULTS and DISCUSSION.....	37
4.1 SEM Images and Reflection Results for Ag NPs.....	37
4.2 Reference Raman Measurement.....	41
4.3 SERS Measurements for Ag NPs and CV/BCB.....	42
4.4 Enhancement Factor Calculations and Results for Ag NPs.....	45
4.5 SEM Images and Reflection Results for Ag NWs.....	53
4.6 SERS Measurements for Ag NWs and CV/BCB.....	57
4.7 Simulation.....	66
5 CONCLUSIONS.....	69
REFERENCES.....	73

LIST OF TABLES

TABLES

Table 3.1: Molecular structure of the dye molecules and their physical characteristics.....	29
Table 4.1: Surface coverage values of Ag NPs for different substrate preparation techniques and 20, 30 and 40 times pass of Ag NP.....	39
Table 4.2: Surface coverage values of Ag NWs for different substrate preparation techniques and 20, 30 and 40 times pass of Ag NWs.....	55

LIST OF FIGURES

FIGURES

- Figure 1.1:** Raman spectrum of (a) Ag electrode dipped into KCl solution, (b) pyridine and KCl solution, (c) pyridine adsorbed on a silver electrode.....3
- Figure 1.2:** Change of the local intensity enhancement in logarithmic scale with respect to incident polarizations: a) 0^0 , b) 30^0 , c) 60^0 and d) 90^0 with the arrows showing different polarizations in the case that plane of the dimers is perpendicular to the incident field.....4
- Figure 1.3:** Fluorescence enhancement for aligned (related to the solid red line on graph and images on the left) and non-aligned (related to the dashed green line on graph and images on the right) fluorescent sphere and Ag dimer, upper images correspond to the AFM topographies with asterisks that are representing the fluorescent spheres, and lower images relate to the fluorescence of these spheres.....5
- Figure 2.1:** Schematic representation of Jablonski diagram illustrating Rayleigh, Stokes and anti-Stokes processes.....7
- Figure 2.2:** Schematic representation of Raman spectroscopy.....9
- Figure 2.3:** (a) Schematic representation of Fresnel diffraction from a single slit, (b) Diffraction pattern relating to Fresnel numbers $N_F=10, 1, 0.5,$ and 0.113
- Figure 2.4:** Schematic representation for distance dependence of magnitude of the near field.....13
- Figure 2.5:** Schematic representation of SERS from molecules (small-blue) adsorbed on metal nanoparticles (large-orange).....14
- Figure 2.6:** (a) Real part and (b) imaginary part of the $\epsilon(\lambda)$ for Ag.....18
- Figure 2.7:** Schematic diagrams of (a) SPPs at the metal/dielectric interface, (b) evanescent fields in the metal and dielectric mediums.....19
- Figure 2.8:** Schematic diagram of localized surface plasmon.....19
- Figure 2.9:** Schematic diagram of cross section of a wire and x-polarized plane wave.....21
- Figure 2.10:** UV-Vis extinction spectrum of colloidal Ag NPs in water.....22

Figure 2.11: UV-Vis extinction spectrum of spray coated Ag NWs on pet substrate and schematic representation of transverse (at shorter wavelengths) mod for Ag NW and longitudinal (at higher wavelengths) surface plasmon mode for Ag nanorods...	23
Figure 2.12: Schematic representation of transverse (a) and longitudinal (b) plasmon modes of a nanowire and dipolar plasmon mode of a nanosphere corresponding to the x- and y- polarized incoming light.....	24
Figure 2.13: Schematic representation of increase in cross section of a nanoparticle under resonant condition.....	25
Figure 2.14: Schematic representation of a molecule (BCB) between hot spot of two Ag NPs.....	26
Figure 3.1: UV-Visible absorption spectrum of CV solution.....	30
Figure 3.2 : UV-Visible absorption spectrum of BCB solution.....	30
Figure 3.3: Concept map illustrating the substrate preparation steps.....	32
Figure 3.4: Experimental setup for spin coating of CV or BCB after spray coating of Ag NW on Si substrates.....	33
Figure 3.5: Schematic diagram of the Raman setup.....	35
Figure 3.6. Schematic diagram of the reflection measurement set-up.....	36
Figure 4.1: Image analysis steps for Ag NP SEM images showing application of denoise filter and marking Ag NPs by threshold.....	37
Figure 4.2: SEM image of 10^{-4} M BCB spin coating on Ag NP spray coating with 20 times pass (middle) and images taken from 4 different locations of it.....	38
Figure 4.3: Total and diffuse reflection spectra of spray coating of in-solution mixed Ag NPs + 10^{-4} M CV for different number of passes.....	40
Figure 4.4: Haze spectrum of spray coating of in-solution mixed Ag NPs + 10^{-4} M CV for different number of passes.....	41
Figure 4.5: Raman intensity spectrum of 10^{-4} M CV liquid droplet on Si wafer.....	42

Figure 4.6: Normalized extinction spectra of Ag NP and Ag NW, and normalized absorption spectra of CV and BCB, green line represents the 532 nm laser wavelength and yellow line represents the scattered light wavelength.....42

Figure 4.7: SERS intensity spectra of spray coating of in-solution mixed Ag NPs + 10^{-4} M CV with 20 times pass obtained from 10 different selected spots of substrate and peak area under a strong peak between the 1600 and 1630 cm^{-1} to be used for statistics of SERS.....43

Figure 4.8: SERS intensity spectra of spray coating of in-solution mixed Ag NPs + 10^{-4} M BCB with 20 times pass obtained from 10 different selected spots of substrate and peak area under a strong peak between the 1395 and 1430 cm^{-1} to be used for statistics of SERS.....44

Figure 4.9: Schematic representation of Raman measurement from a droplet of 10^{-4} M CV molecule.....45

Figure 4.10: Schematic representation of SERS measurement for EF calculation...46

Figure 4.11: Corresponding values and ranges for box charts.....47

Figure 4.12: An example of data distribution for box charts.....47

Figure 4.13: Box charts displaying the statistics of SERS measurements and enhancement factor for (a) Ag NP spray coating and 10^{-4} M CV solution spin coating, (b) spray coating of in-solution mixed Ag NPs + 10^{-4} M CV, (c) Ag NP spray coating and 10^{-4} M BCB solution spin coating, (d) spray coating of in-solution mixed Ag NPs + 10^{-4} M BCB.....48

Figure 4.14: Box charts displaying the statistics of SERS measurements and enhancement factor for (a) Ag NP spray coating and 10^{-5} M CV solution spin coating, (b) spray coating of in-solution mixed Ag NPs + 10^{-5} M CV, (c) Ag NP spray coating and 10^{-5} M BCB solution spin coating, (d) spray coating of in-solution mixed Ag NPs + 10^{-5} M BCB.....49

Figure 4.15: Box charts displaying the statistics of SERS measurements and enhancement factor for (a) Ag NP spray coating and 10^{-6} M CV solution spin coating, (b) spray coating of in-solution mixed Ag NPs + 10^{-6} M CV, (c) Ag NP

spray coating and 10^{-6} M BCB solution spin coating, (d) spray coating of in-solution mixed Ag NPs + 10^{-6} M BCB.....	50
Figure 4.16: Mean SERS intensity obtained from box charts and linear fit of Ag NP spray coating and 10^{-4} , 10^{-5} , 10^{-6} M CV solution spin coating.....	51
Figure 4.17: Mean SERS intensity obtained from box charts and linear fit of spray coating of in-solution mixed Ag NPs + 10^{-4} , 10^{-5} , 10^{-6} M CV.....	51
Figure 4.18: Mean SERS intensity obtained from box charts and linear fit of Ag NP spray coating and 10^{-4} , 10^{-5} , 10^{-6} M BCB solution spin coating.....	52
Figure 4.19: Mean SERS intensity obtained from box charts and linear fit of spray coating of in-solution mixed Ag NPs + 10^{-4} , 10^{-5} , 10^{-6} M BCB.....	52
Figure 4.20: SEM image of 10^{-4} M CV spin coating on Ag NW spray coating with 20 times pass (middle) and images taken from 4 different locations of it.....	53
Figure 4.21: SEM image of spray coating of in-solution mixed Ag NWs with 20 times pass + 10^{-4} M BCB (middle) and images taken from 4 different locations of it.....	54
Figure 4.22: Approximated length of Ag NWs measured from SEM image of spray coating of colloidal Ag NWs with 30 times pass number and 10^{-4} M BCB spin coating.....	55
Figure 4.23: Total and diffuse reflection spectra of spray coating of in-solution mixed Ag NWs + 10^{-4} M CV for different number of passes.....	56
Figure 4.24: Haze spectrum of spray coating of in-solution mixed Ag NWs + 10^{-4} M CV for different number of passes.....	57
Figure 4.25: SERS intensity spectra of Ag NW spray coating with 20 times pass and 10^{-4} M CV spin coating obtained from 10 different selected spots of substrate and peak area under a strong peak between the 1600 and 1630 cm^{-1} to be used for statistics of SERS.....	58
Figure 4.26: SERS intensity spectra of Ag NW spray coating with 20 times pass number and 10^{-4} M BCB spin coating obtained from 10 different selected spots of	

substrate and peak area under a strong peak between the 1395 and 1430 cm^{-1} to be used for statistics of SERS.....59

Figure 4.27: Box charts displaying the statistics of SERS measurements for (a) Ag NW spray coating and 10^{-4} M CV solution spin coating, (b) Ag NW spray coating and 10^{-4} M BCB solution spin coating.....60

Figure 4.28: Box charts displaying the statistics of SERS measurements for (a) spray coating of in-solution mixed Ag NWs + 10^{-4} M CV, (b) spray coating of in-solution mixed Ag NWs + 10^{-4} M BCB.....60

Figure 4.29: Box charts displaying the statistics of SERS measurements for (a) Ag NW spray coating and 10^{-5} M CV solution spin coating, (b) Ag NW spray coating and 10^{-5} M BCB solution spin coating.....61

Figure 4.30: Box charts displaying the statistics of SERS measurements for (a) spray coating of in-solution mixed Ag NWs + 10^{-5} M CV, (b) spray coating of in-solution mixed Ag NWs + 10^{-5} M BCB.....62

Figure 4.31: Box charts displaying the statistics of SERS measurements for (a) Ag NW spray coating and 10^{-6} M CV solution spin coating, (b) Ag NW spray coating and 10^{-6} M BCB solution spin coating.....63

Figure 4.32: Box charts displaying the statistics of SERS measurements for (a) spray coating of in-solution mixed Ag NWs + 10^{-6} M CV, (b) spray coating of in-solution mixed Ag NWs + 10^{-6} M BCB.....63

Figure 4.33: Mean SERS intensity obtained from box charts and linear fit of Ag NW spray coating and 10^{-4} , 10^{-5} , 10^{-6} M CV solution spin coating.....64

Figure 4.34: Mean SERS intensity obtained from box charts and linear fit of spray coating of in-solution mixed Ag NWs + 10^{-4} , 10^{-5} , 10^{-6} M CV.....65

Figure 4.35: Mean SERS intensity obtained from box charts and linear fit of Ag NW spray coating and 10^{-4} , 10^{-5} , 10^{-6} M BCB solution spin coating.....65

Figure 4.36: Mean SERS intensity obtained from box charts and linear fit of spray coating of in-solution mixed Ag NWs + 10^{-4} , 10^{-5} , 10^{-6} M BCB.....66

Figure 4.37: Electric field distribution of a 100 nm dimer obtained by locating (a) 20, (b) 10, (c) 5, (d) 2 nm away from each other.....67

Figure 4.38: Enhancement factor graph for dimers (radius of 50 nm) located on a 400 x 400 mesh grid at a distance of 2, 5, 10,20 and 50 nm from each other.....68

CHAPTER 1

INTRODUCTION

The scope of this thesis is to obtain versatile statistical data for surface enhanced Raman scattering (SERS) that is a localized surface plasmon (LSP) application. SERS allows effective detection of analytes attached to the metal nanostructures through an enhancement mechanism. Statistics of SERS intensities and corresponding enhancement factors (EFs) of the same level as the highest values recorded in the literature using polyol synthesized colloidal silver nanoparticles (Ag NPs) and silver nanowires (Ag NWs) that have well-documented and promising plasmonic properties are presented.

Molecular sensing, identification and quantification is essential for pathogen or cancer discovery in biological liquids [1]. Several well-established test assays are in use for decades based on fluorescence and surface plasmon resonance (SPR). Most of these detection techniques rely on the use of labels/molecular markers specifically designed for target molecules such as proteins, peptides, DNA and RNA [2]. So the test kits must necessarily be fabricated for the set of target molecules and they cannot be used in detection of other molecules that may exist in the biological analyte. In fact existence of bystander molecules is not desired in the analyte in order to minimize interference. As these techniques are based on secondary effects of the target molecules presence, the information arrives indirectly from reporters rather than the molecules themselves [3]. However, direct spectroscopic investigation of the analyte can prove to provide much more detailed information both on the presence of molecules and their relative amounts with chemical states. This is because the information in this kind of label-free, spectroscopic technique arrive directly from the target and bystander molecules in the analyte [4]. Despite the mentioned advantage of using spectroscopic technique in molecular detection, its wide range utilization has been limited because of the low signal levels. These levels can only be

detected using high-cost and highly complex instrumentation, which are barely portable [5]. An unexpected phenomenon called “surface enhancement”, of which the physical mechanisms have only been partially understood, has come to the aid of spectroscopy. By using surface enhancement effect of certain class of material surfaces, molecular fluorescence and Raman spectroscopic signals had been boosted to unprecedentedly high levels, almost to the standard microscopic signal levels. In fact, we owe the discovery of surface enhancement effect to Raman spectroscopy examinations of electrodeposited molecules on the metal electrode surfaces [1], [6],[7], [8]. Afterwards, the effect was historically named as “surface enhanced Raman scattering” [9].

In this thesis work, the SERS activity of adsorbed molecules on metal nanostructures was demonstrated. It is possible to enhance the incident and scattering electric fields by taking advantage of the roughness of the surface and near field effects. At this stage, it is necessary to indicate the developments that make SERS a very effective area, starting with the discovery of Raman effect.

In 1921, Chandrasekhara Venkata Raman discovered a new type of light scattering by focusing a beam of sunlight with a telescope onto the samples and detecting the modified scattered light through light-filters [10]. In 1930, he won the Nobel prize for his discovery of phenomena that is today called as Raman scattering named after him and his researches on the diffusion of gasses.

Raman spectroscopy was developed rapidly through the invention of lasers as intense excitation sources. In the early 1970s infrared spectroscopy was proceeding to obtain vibrational spectra from a monolayer of adsorbed molecules on solid surfaces. Raman spectroscopy was not adequate to fill this need because of the weak signal intensities after some confirmations of limited detections related to Raman measurements using planar metal electrodes, in 1974 Fleishmann et al. revealed Raman spectra of pyridine adsorbed at an electrochemically roughened silver (Ag) electrode in an aqueous electrolyte solution. They increased the surface area by a factor greater than 10 by cyclic linear potential sweeping for 15 minutes [11]. They reached intensity values about 500–1000 counts per second using a 100 mW (514.5 nm) argon ion laser light. These unexpected strong Raman signals were attributed to

the increased number of adsorbed molecules as a result of increased surface area of the electrodes [12].

Following this publication, some researchers investigated the relationship between surface area and Raman signals to highlight the unanswered questions by adsorbing pyridine on roughened Ag electrodes. It was revealed that such observed high Raman signals can not be resulted from the increased surface area. In 1977 M. G. Albrecht and Alan Creighton obtained enhanced signals by a factor of 10^5 – 10^6 from pyridine compared with the result in the absence of Ag. This enhancement was attributed to increased molecular Raman scattering cross sections. They also emphasized the resonant Raman scattering through the suggestions of Philpott [7]. Richard Van Duyne and his graduate student David Jeanmaire introduced the increase of electromagnetic field as the reason of enhancement that they observed in their similar studies [12].

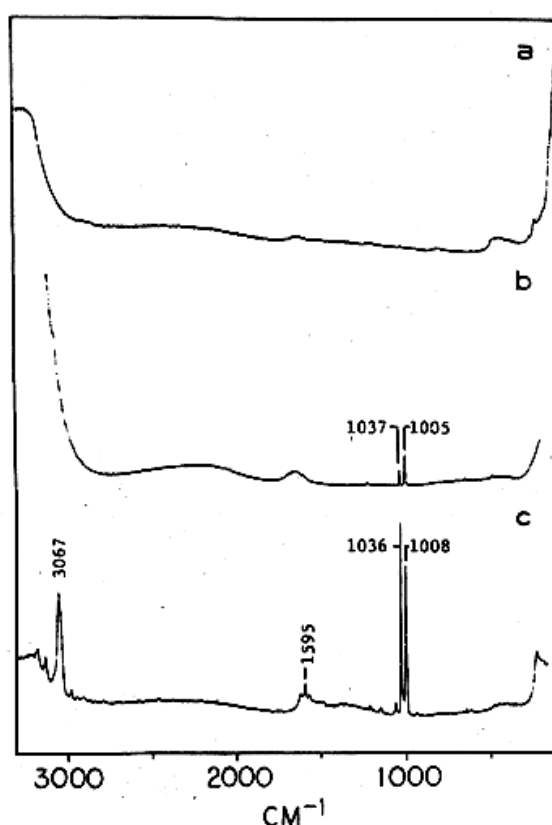


Figure 1.1: Raman spectrum of (a) Ag electrode dipped into KCl solution, (b) pyridine and KCl solution, (c) pyridine adsorbed on a Ag electrode [6].

In Figure 1.1, Raman spectrum of (a) Ag electrode dipped into potassium chloride (KCl), (b) mixture of aqueous pyridine and KCl, (c) adsorbed pyridine on Ag electrode from a bulk solution of pyridine and KCl are presented. It can be concluded that peaks at (c) are more intense than that of (b) and some peaks that do not consist in (b) are seen in (c) that are attributed to the consisting of active sites on electrode surfaces [6]. In the following years, innovations in Raman instrumentation have enabled the study of Raman to be interdisciplinary, where, physicists, chemists, biologists and engineers utilize. Improvements in nanoscience and nanotechnology enabled SERS effect to be investigated by plasmonics effectively [9]. In 1997 K. Kneipp et al. observed influence of a single molecule in Raman scattering for the first time by taking advantage of excessively large cross sections (10^{-17} - 10^{-16} $\text{cm}^2/\text{molecule}$) [13].

In some researches, effect of polarization of the electromagnetic field on particles that are located close to each other was investigated. It was explored that local intensity enhancement is strongly dependent on the incident polarization due to the surface plasmon mode coupling between closely located metal nanostructures.

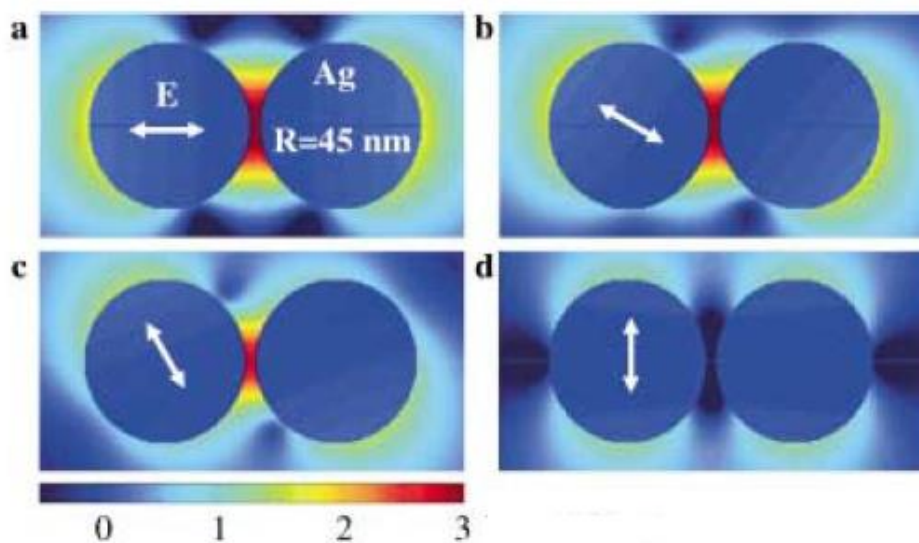


Figure 1.2: Change of the local intensity enhancement in logarithmic scale with respect to incident polarizations: a) 0° , b) 30° , c) 60° and d) 90° with the arrows showing different polarizations in the case that plane of the dimers is perpendicular to the incident field [14].

Maximum enhancement of electromagnetic field is obtained when polarization of incident light is parallel to the axis of dimers, whereas perpendicular polarization does not lead to an enhancement between dimers with radius 45 nm and distance 5 nm as shown in Figure 1.2 [14]. Investigations regarding fluorescence enhancement also provides important contributions to the characteristic hot spots and field enhancement. When the fluorescent sphere is located in the hot spot of a Ag dimer so that all three are aligned within the same line as shown in atomic force microscope (AFM) topographical image on the left and fluorescence image on the lower of it in Figure 1.3, strong fluorescence enhancement is obtained that is represented as solid red line on the graph. If this straight alignment is not provided so that the dimer can not benefit from hot spot effect as shown in AFM topographical image on the right and fluorescence image on the lower of it, fluorescence enhancement decreases as compared to the previous case, as shown in graph with dashed green line [15].

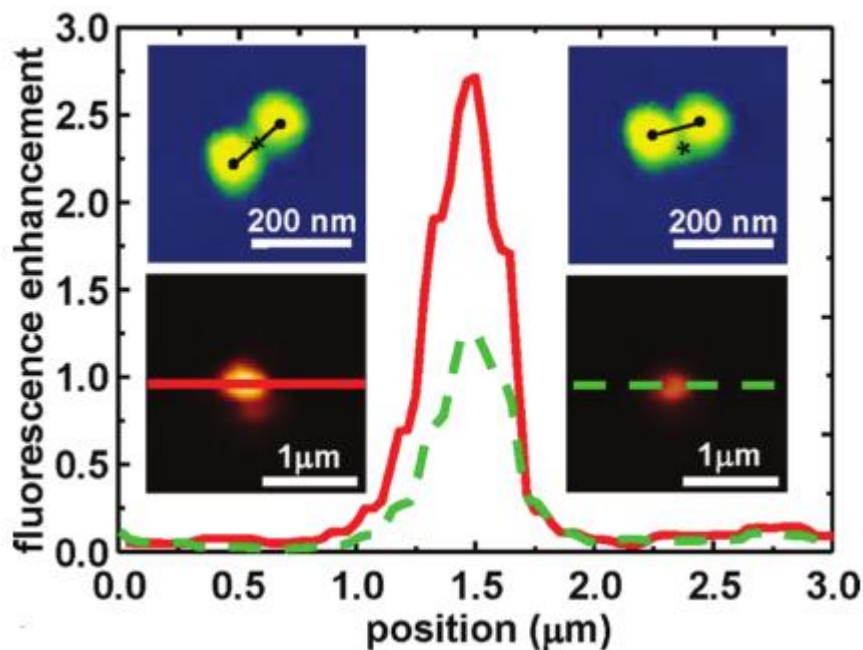


Figure 1.3: Fluorescence enhancement for aligned (related to the solid red line on graph and images on the left) and non-aligned (related to the dashed green line on graph and images on the right) fluorescent sphere and Ag dimer, upper images correspond to the AFM topographies with asterisks that are representing the fluorescent spheres, and lower images relate to the fluorescence of these spheres

[15].

In recent years, hot topics of SERS are electromagnetic enhancement at hot spots, chemical enhancement mechanism, methods to fabrication of homogenous and reproducible SERS substrates, resonance and polarization studies.

In the light of the introduced strong SERS activity at the hot-spots formed between metal nanoparticles, Controlled experiments on solution synthesized Ag NPs and Ag NWs were performed. The literature on use of Ag NPs in Raman enhancement is already very rich [9]; however the chosen Ag nanostructures for this thesis have several distinct properties that result in extremely strong field localization and enhancement of Raman signals for the attached molecules.

CHAPTER 2

THEORY

2.1. Raman Scattering

In scattering process, an incident photon experiences simultaneous absorption and another photon is emitted that is called as scattered photon. There are two types of scattering processes that are elastic and inelastic scattering. Elastic scattering that is also called as Rayleigh scattering corresponds with the same energy of the incoming and scattered photons. In fact, after scattering process, the molecule remains at the same energy level. However, if energy of the incoming and scattered photons is not the same after the scattering process, this case is called as inelastic scattering, in the concept of this study with being Raman scattering.

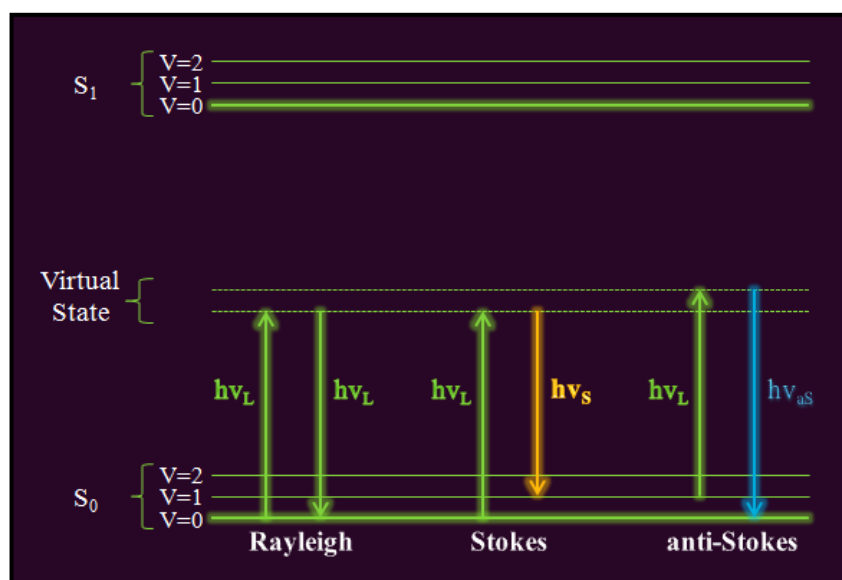


Figure 2.1: Schematic representation of Jablonski diagram illustrating Rayleigh, Stokes and anti-Stokes processes.

In Figure 2.1, Jablonski energy diagram illustrates the quantum mechanical approach of the Raman scattering. If molecule is excited from the vibrational ground state $\nu = 0$ to the first excited state $\nu = 1$, this case is called as Stokes process that corresponds to the energy decrease of the molecule as much as $h\nu_s = h\nu_L - h\nu_\nu$; if molecule relaxes from excited state to the ground state, this case is called as anti-Stokes process, with energy increase of the molecule being $h\nu_{as} = h\nu_L + h\nu_\nu$ [9], [16].

Only a small fraction (1×10^{-7}) of the photons is inelastically scattered and because the probability of Stokes process at room temperature is higher compared to the anti-Stokes process, intensity of Stokes scattered photons is higher [17].

Electric field of the beam in the case of an interaction of a molecule and incident light with vibrational frequency ν_0 is defined as in the following form:

$$\mathbf{E} = \mathbf{E}_0 \cdot \cos(2\pi \cdot \nu_0 \cdot t) \quad (2.1)$$

This electric field induces a dipole moment \mathbf{p} that is defined as in the following form:

$$\mathbf{p} = \alpha \cdot \mathbf{E} + \frac{1}{2} \cdot \beta \cdot \mathbf{E}^2 + \frac{1}{6} \cdot \gamma \cdot \mathbf{E}^3 + \dots \quad (2.2)$$

where α , β , γ are polarizability tensors. In most cases β and γ are neglected due to the small values of them compared to that of α [18].

In order to a molecule be Raman active, the polarizability tensor should change during the vibration as a function of normal coordinate of the molecule as indicated below:

$$\alpha = \alpha_0 + \sum_k \left(\frac{\partial \alpha}{\partial Q_k} \right)_0 \cdot Q_k + \dots \quad (2.3)$$

Where α_0 is the polarizability of the bonds where the distance between the nuclei in equilibrium. Q_k is normal coordinate of the k^{th} normal vibration related to the vibrational frequency ν_k . If only ν^{th} normal vibration is considered in this series and other terms are neglected by harmonic oscillation approximation, polarizability is defined as:

$$\alpha_v = \alpha_0 + \frac{\partial \alpha}{\partial Q_v} \cdot Q_v \quad (2.4)$$

Hence, induced dipole moment is obtained as:

$$\mathbf{p} = \mathbf{p}(v_0) + \mathbf{p}(v_0 + v_v) + \mathbf{p}(v_0 - v_v) \quad (2.5)$$

where the first term is related to the Rayleigh scattering, second term is related to the anti-Stokes scattering and the third term corresponds to the Stokes scattering.

The condition for observing Raman effect is that α'_v is nonzero that means that polarizability should change in the event of the normal vibration. If the polarizability of the molecule changes, the vibration is Raman active and in case the dipole moment changes, the vibration is infrared active. In the case of a homonuclear diatomic molecule (i.e. H_2), change in the internuclear distance contribute to the change of the polarizability of the molecule and consequently the vibration is Raman active. In a heteronuclear diatomic molecule (i.e. HCl), charge separation causes the dipole moment to change and thus the vibration is infrared active. At the same time it is infrared active due to the bond distance dependence of the polarizability. In triatomic molecules, linear (CO_2) and nonlinear (H_2O) molecules should be considered separately whereas in complex molecules determination of Raman or infrared activity is not so straightforward; in fact quantum mechanics and group theory is applied.

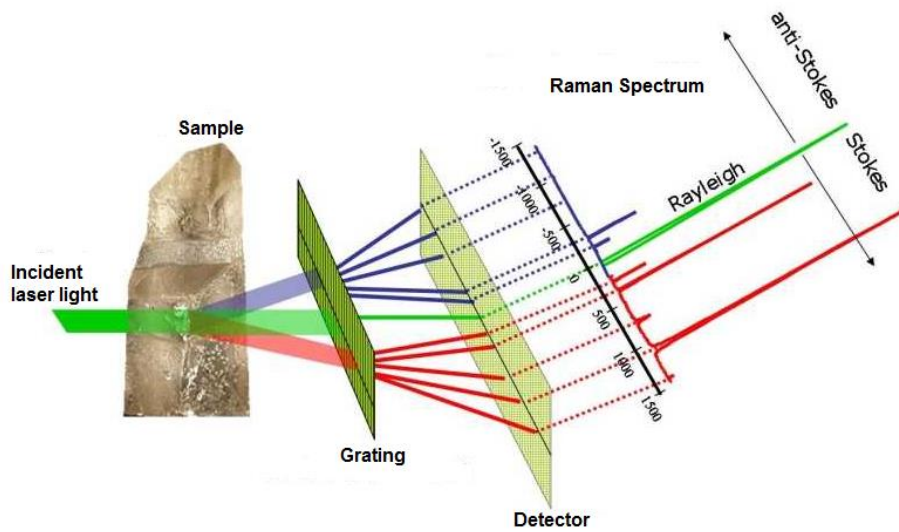


Figure 2.2: Schematic representation of Raman spectroscopy [19].

In Raman spectroscopy as illustrated in Figure 2.2, generally a laser beam is focused on the sample and scattered radiation and obtained spectrum represents Raman intensity as a function of w that corresponds to the difference between the scattered and incident radiation frequency:

$$w = \bar{\nu}_m - \bar{\nu}_0 = \frac{\nu_m}{c} - \frac{\nu_0}{c} \quad (2.6)$$

where ν_m and ν_0 (in units of cm^{-1}) correspond to the scattered and incident light frequency, respectively and c is the speed of light. Raman shift is positive for Stokes process and negative for anti-Stokes process.

To determine the vibrational frequency of the molecule, harmonic oscillation approximation is used and thus the following relation is obtained as;

$$\nu_v = \frac{1}{2\pi} \cdot \sqrt{\frac{\kappa}{\mu}} \quad (2.7)$$

where κ is the force constant of the bond and μ is the reduced mass that is defined as in the following form for a diatomic molecule;

$$\frac{1}{\mu} = \frac{1}{m_1} + \frac{1}{m_2} \quad (2.8)$$

where m_1 and m_2 are the masses of the atoms. It can be concluded that the Raman band position is dependent on the force constant of the bond, the reduced mass and also selection rules as mentioned before.

To obtain the Raman spectrum of the organic molecules, it is needed to consider the group frequencies that are regarding the vibrations of series of functional group by neglecting the other vibrations in the molecule.

The intensity of scattered light is defined as the change in electromagnetic flux over corresponding solid angle:

$$I = \frac{d\Phi}{d\Omega} = \frac{\pi^2 \cdot c \cdot \bar{\nu}^4 \cdot p_0^2 \cdot \sin^2 \theta}{2 \cdot \epsilon_0} \quad (2.9)$$

where $\bar{\nu}$ is the absolute wavenumber of the electromagnetic radiation, p_0 is the amplitude of the induced oscillating dipole moment, c is the speed of light, ϵ_0 is the permittivity of the vacuum and θ is the angle between the dipole moment and measurement direction that is integrated over a solid angle centered around θ [18].

In spontaneous Raman scattering that is a linear process, power of inelastically scattered light (particularly for Stokes process) is defined as:

$$P_S(\nu_S) = N\sigma_{RS}I(\nu_L) \quad (2.10)$$

where N is the number of scatterers within the probed volume, σ_{RS} is the Raman cross section and $I(\nu_L)$ is the intensity of incident beam of light [16], [20].

2.2. Enhancement Mechanism

SERS is an application of far-field detection through the use of near-field properties of probed volume [9], therefore it is necessary to indicate the theoretical background of these fields.

Heisenberg's uncertainty relation indicates the following relation:

$$\Delta x \geq \frac{1}{2\Delta k_i} \quad (2.11)$$

where Δx and Δk_i refer to the uncertainty in the position in a certain direction and wavevector of a photon, respectively, with $k_i = \sqrt{k_x^2 + k_y^2 + k_z^2}$ and $k_i = \frac{2\pi}{\lambda_i}$. A similar representation to the Rayleigh diffraction limit is achieved by substituting k_i into the equation 2.11 [21]:

$$\Delta x \geq \frac{\lambda}{4\pi} \quad (2.12)$$

Freely propagating waves are considered in far-field applications. Positional uncertainty for far-field is defined as:

$$\Delta x \geq \frac{1}{k_x} = \frac{\lambda_i}{2\pi} \quad (2.13)$$

where k_x is real.

On the other hand, evanescent fields provide opportunity to study the near-field in virtue of imaginary part of the wavevector where exponentially decaying occurs. Wavevector(s) in other direction(s) can be larger than the aforementioned wavevector k_i . As a result, positional uncertainty lose validity in this situation and can be smaller than the value of $\lambda/2\pi$ [22].

Diffraction limit in focusing objective point of view is expressed as follows:

$$d_{\text{sep}} = \frac{0,61\lambda}{NA} \quad (2.14)$$

where d_{sep} is the distance between two points that can be resolved, λ is the wavelength and NA is the numerical aperture of the microscope objective. Far field optical applications do not allow this limit to be exceeded [23]. The disadvantage of this limit in terms of SERS is that the properties of the nanoparticles can not be obtained in detail.

One of the most frequently addressed topics on nano-optics is to provide access beyond the diffraction limit of the light by focusing the light into confined area that allows for the characterization and modification in nanometer scale [21], [22]. In 1928, Syngé came up with the idea of near-field optical microscopy. The idea was putting a nontransparent plate in the vicinity of a substrate and trying for a high spatial resolution of spot that is beyond the diffraction limit of light by illuminating it from one side. It was indicated that resolution of acquired image had not been limited by wavelength of light but the size of the aperture. In 1972, Ash and Nichols acquired resolution of $\lambda/60$ by using 1.5 mm aperture. The discovery of scanning probe microscopy was an important development for near-field studies. In 1984, a significant development was achieved and International Business Machines revealed sub-wavelength images for the first time. These developments in near-field provided a basis for investigation of plasmonics [21].

Fraunhofer, called also as far-field, diffraction corresponds to the fact that the incident plane wave is send through an aperture that is far away from the observation

plane. However, Fresnel, called also as near-field, diffraction is considered when curvature nature of the diffracted wave is present as illustrated in Figure 2.3 [24].

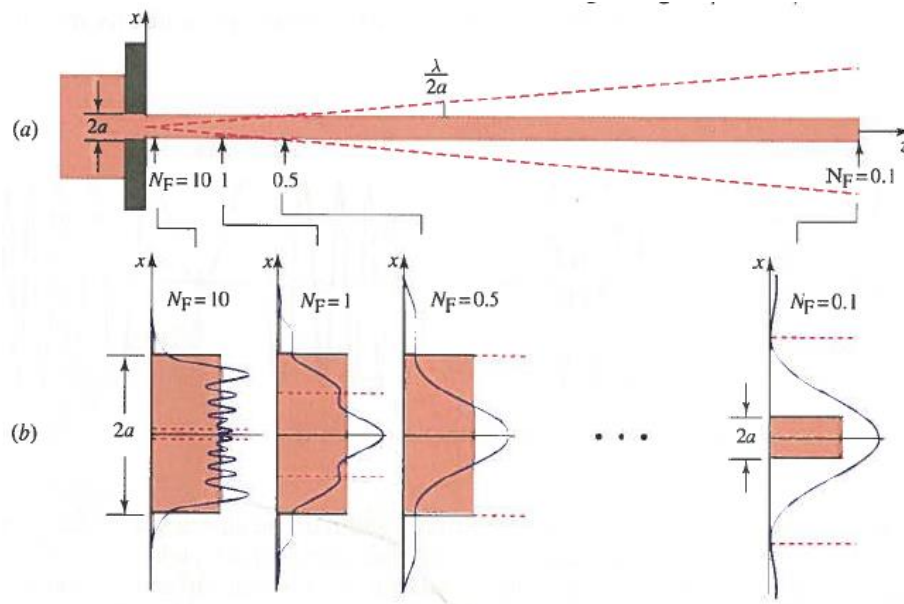


Figure 2.3: (a) Schematic representation of Fresnel diffraction from a single slit, (b) Diffraction pattern relating to Fresnel numbers $N_F=10, 1, 0.5,$ and 0.1 [25].

N_F corresponds to the Fresnel number. If N_F is very large leading to the small distance from the aperture, diffraction pattern is obtained as shadow of the slit. At larger distances, Fraunhofer behavior is presented [25].

The field in the vicinity of an excited molecular dipole is inversely proportional to the third power of the distance d as shown in Figure 2.4 [22].

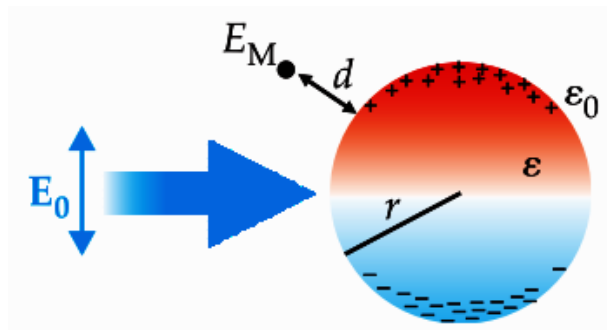


Figure 2.4: Schematic representation for distance dependence of magnitude of the near field [16].

The exponentially decaying fields that will be discussed in more detail in the following sections are an application of near-fields.

2.3. Surface Enhanced Raman Scattering

SERS is a technique that overcomes small scattering cross section of NRS through taking advantage of the plasmonic properties of the metal nanostructures that are excited by a monochromatic light source. Hence, it provides excessively low concentration of molecules to be detected [26]. Figure 2.5 represents the SERS process by showing energy change of incident light through interaction of incoming beam and the molecules adsorbed onto metal nanostructures.

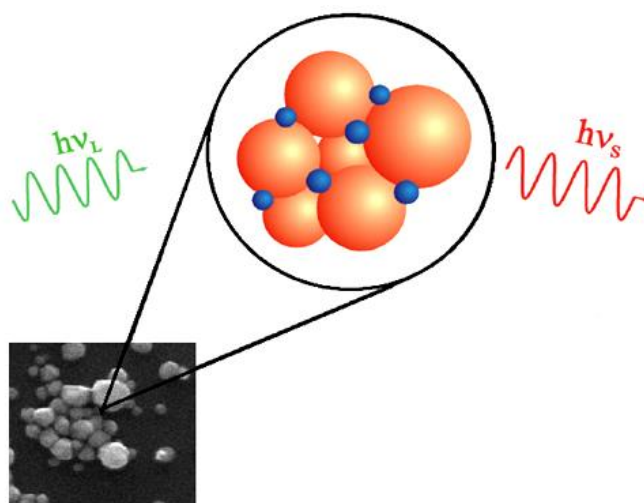


Figure 2.5: Schematic representation of SERS from molecules (small-blue) adsorbed on metal nanoparticles (large-orange) [16].

Two mechanisms are responsible for the enhancement mechanism in SERS, namely, electromagnetic and chemical enhancement.

2.3.1. Electromagnetic-Field Enhancement

It is necessary to indicate the interaction of electromagnetic field with metals to form a basis for understanding electromagnetic-field enhancement that correlates with

plasmon resonances [9]. In fact, excitation of the localized surface plasmons (LSPR) is the basis for this enhancement by increasing the intensity of incident and inelastically scattered fields [16], [20].

The electromagnetic effect will be much stronger compared to the chemical effect when the frequency of light does not correlate with the electronic transition of the molecule [27].

When the incident field, scattered field and SP are in resonance with each other, excessively strong field enhancement is observed in the close proximity of the metal nanostructures. SPs that are excited by incident beam of light causes dipolar field radiation. Interaction of incident and dipolar fields leads to enhancement of the electric field in the vicinity of metal structures. Hence, inelastically scattered field is also enhanced. [16]. Investigating optical properties of the noble metals is important to interpretation of electromagnetic-field enhancement mechanism.

2.3.1.1. Optical Properties of Noble Metals

Macroscopic Maxwell equations should be indicated to reveal interaction of metals and electromagnetic fields. This approximation is governed by averaging the microscopic fields through the larger length scales than the lattice spacing[20], [9].

$$\nabla \cdot \mathbf{D} = \rho_{ext} \quad (2.15)$$

$$\nabla \cdot \mathbf{B} = 0 \quad (2.16)$$

$$\nabla \times \mathbf{E} = - \frac{\partial \mathbf{B}}{\partial t} \quad (2.17)$$

$$\nabla \times \mathbf{H} = \mathbf{J}_{ext} + \frac{\partial \mathbf{D}}{\partial t} \quad (2.18)$$

\mathbf{D} (dielectric displacement), \mathbf{E} (electric field), \mathbf{H} (magnetic field), and \mathbf{B} (magnetic induction or magnetic flux density) in these equations are related with polarization \mathbf{P} and magnetization \mathbf{M} in the following form:

$$\mathbf{D} = \varepsilon_0 \mathbf{E} + \mathbf{P} \quad (2.19)$$

$$\mathbf{H} = \frac{1}{\mu_0} \mathbf{B} - \mathbf{M}, \quad (2.20)$$

where ϵ_0 is the electric permittivity and μ_0 is the magnetic permeability of vacuum. These relations take the following form when linear, isotropic and non-magnetic media conditions are considered:

$$\mathbf{D} = \epsilon_0 \epsilon \mathbf{E} \quad (2.21)$$

$$\mathbf{B} = \mu_0 \mathbf{H} \quad (2.22)$$

where dielectric constant is dependent on frequency $\epsilon = \epsilon(\omega)$ that will be discussed later in detail.

Free conduction electrons of metals such as Ag, gold (Au), copper (Cu) and aluminum (Al) ensure these noble metals that reflect light in the visible range of the spectrum influentially. Unique properties of these metals that are different from other dielectric materials might well explained by the concepts of free electron plasma or solid plasma [9].

The optical properties of metals are achieved by free-electron gas model that can be explained by motion of free electrons in a fixed positive ions background by not taking into account the vibrations of ions. This model is valid up to the ultraviolet range of the spectrum for alkali metals and at visible range of the spectrum for noble metals [9], [20].

After the oscillation of electrons due to interaction with the electromagnetic field, collisions cause their oscillation to damp with an inverse of the relaxation time of the free electron gas called as characteristic collision frequency $\gamma = 1/\tau$.

When electric field is applied to the electrons in the x coordinate in equilibrium, equation of motion is as follows [28] :

$$m\ddot{\mathbf{x}} + m\gamma\dot{\mathbf{x}} + m\omega_0^2\mathbf{x} = -e\mathbf{E}. \quad (2.23)$$

Drude model provides us with describing optical response of atoms and molecules by using Lorentz model through ignoring restoring force that is characterized by

resonance frequency (ω_0). The reason of taking $\omega_0 = 0$ is because of that conduction electrons are not bound in a metal [9]. Then for an electron of the plasma sea, equation of motion takes the form:

$$m\ddot{\mathbf{x}} + m\gamma\dot{\mathbf{x}} = -e\mathbf{E}. \quad (2.24)$$

This equation can be solved by taking $\mathbf{E}(t) = \mathbf{E}_0 e^{-i\omega t}$, oscillation of the electron is described by:

$$\mathbf{x}(t) = \mathbf{x}_0 e^{-i\omega t} \quad (2.25)$$

\mathbf{x}_0 is a complex amplitude and $\mathbf{x}(t)$ can therefore be written as:

$$\mathbf{x}(t) = \frac{e}{m(\omega^2 + i\gamma\omega)} \mathbf{E}(t). \quad (2.26)$$

Considering the macroscopic polarization $\mathbf{P} = -ne\mathbf{x}$, the following form is obtained:

$$\mathbf{P} = -\frac{ne^2}{m(\omega^2 + i\gamma\omega)} \mathbf{E}. \quad (2.27)$$

If this expression is put into equation $\mathbf{D} = \epsilon_0 \mathbf{E} + \mathbf{P}$, \mathbf{D} can be written as:

$$\mathbf{D} = \epsilon_0 \left(1 - \frac{ne^2}{m(\omega^2 + i\gamma\omega)} \right) \mathbf{E}, \quad (2.28)$$

where $\omega_p^2 = \frac{ne^2}{\epsilon_0 m}$ is called as plasma frequency.

Finally, the dielectric function of the free electron gas is given by:

$$\epsilon(\omega) = 1 - \frac{\omega_p^2}{\omega^2 + i\gamma\omega} \quad (2.29)$$

Real and imaginary parts of the $\epsilon(\omega)$ are in the following forms:

$$\text{Re}(\epsilon(\omega)) = 1 - \frac{\omega_p^2}{\omega^2 + \gamma^2} \quad (2.30)$$

$$\text{Im}(\epsilon(\omega)) = \frac{\omega_p^2 \gamma}{\omega(\omega^2 + \gamma^2)} \quad (2.31)$$

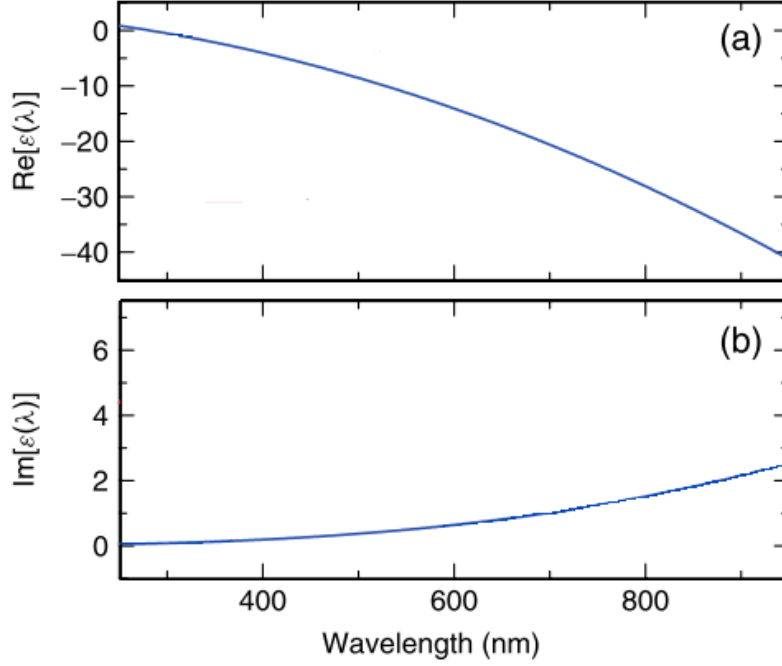


Figure 2.6: (a) Real part and (b) imaginary part of the $\epsilon(\lambda)$ for Ag [29].

It can be seen also from the Figure 2.6 (a) that when the frequency is limited as $\omega < \omega_p$, $\text{Re}(\epsilon(\omega))$ becomes smaller than zero. Another significant property that can be acquired from these expressions is that $\text{Im}(\epsilon(\omega))$ is small provided that ω is not too small as represented in Figure 2.6 (b). The metals that satisfy the conditions of negativity of the $\text{Re}(\epsilon(\omega))$ and small value of the $\text{Im}(\epsilon(\omega))$ in the range of interest ensure that they are appropriate for the study of plasmonics. Another interpretation that can be gained from Figure 2.6 is that imaginary part of the dielectric function gives information about the absorption of Ag [29], and real part of the dielectric function relates to the reflection [30].

2.3.1.2. Surface Plasmons

Electromagnetic excitations that propagate along the metal/dielectric interface are called as surface plasmon (SP) but they are called as surface plasmon polaritons in the case of retardation effects should be considered due to plasmon and photon share the energy [9], [20], [31]. SPs enable excitation light to focus and control in the sub-wavelength scale [32].

Shape of the metal nanostructure and dielectric function of the medium that are indicated in previous section are essential contributors to establish the SPR frequency [32], [30]. In resonance conditions, SPs propagate in the x and y directions as illustrated in Figure 2.7 (a) and decay evanescently in z direction as illustrated in Figure 2.7 (b) [33]. δ_d and δ_m correspond to the evanescent field length in the dielectric and metal medium, respectively.

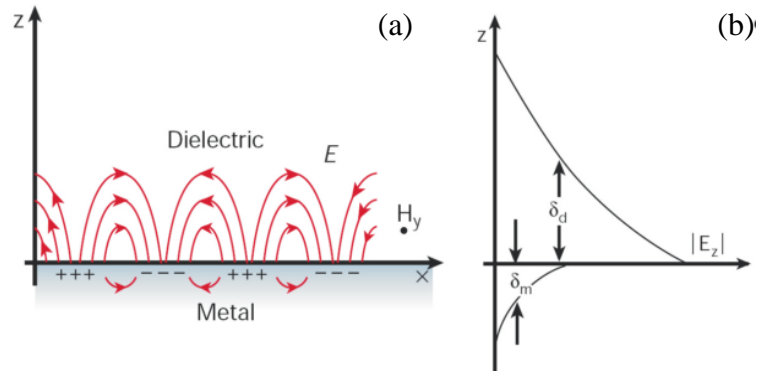


Figure 2.7: Schematic diagrams of (a) SPPs at the metal/dielectric interface, (b) evanescent fields in the metal and dielectric mediums [31].

2.3.1.3. Localized Surface Plasmons

In the case of the LSP, size of the nanoparticle is much smaller than the wavelength of the incident field and plasmon oscillates locally around the nanoparticle as shown in Figure 2.8. Frequency of this oscillation is called as LSPR. It is affected by dielectric function of the medium as in SPR; however, sensing volume of LSPR is confined in a much more smaller area than that of SPR [33]. In fact, it encloses up to 1-2 nanometers away from the surface [29].

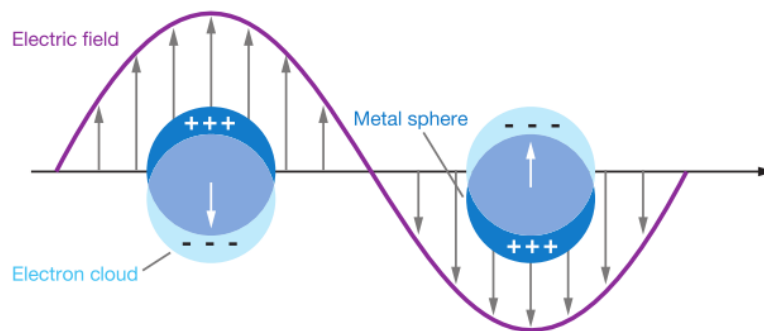


Figure 2.8: Schematic diagram of localized surface plasmon [33].

Quasi-static approximation that corresponds to neglecting retardation effect is used to electromagnetic mode analysis of nanoparticles and nanowires that are smaller than wavelength of incident field in size. [21]. Electric field of an oscillating dipole is

$$\mathbf{E}(\mathbf{r}, t) = \frac{1}{4\pi\epsilon_0} \left[k^2 (\mathbf{n} \times \boldsymbol{\mu}) \times \mathbf{n} \frac{e^{ikr}}{r} + [3\mathbf{n}(\mathbf{n} \cdot \boldsymbol{\mu}) - \boldsymbol{\mu}] \left(\frac{1}{r^3} - \frac{ik}{r^2} \right) e^{ikr} \right] e^{i\omega t} \quad (2.32)$$

Where $\boldsymbol{\mu}$ is the dipole moment and by assuming that $kr \ll 1$ in the near field zone, the electrostatic field of a point dipole is obtained as follows;

$$\mathbf{E}(\mathbf{r}, t) = \frac{1}{4\pi\epsilon_0} [3\mathbf{n}(\mathbf{n} \cdot \boldsymbol{\mu}) - \boldsymbol{\mu}] \frac{e^{i\omega t}}{r^3} \quad (2.33)$$

where $e^{i\omega t}$ corresponds to oscillation of point dipole solely in time. Analysis of electromagnetic field also requires the Laplace equation and appropriate boundary conditions.

It is crucial to determine how the resonance changes with respect to geometry, within the scope of this study characteristic resonance behavior of a metal nanowire and a nanoparticle is going to be investigated.

In the case of a wire whose length divided by radius a is much larger than 1 and being impinged by an x-polarized electromagnetic wave that is illustrated in the Figure 2.9, solution of the electric field $\mathbf{E} = -\nabla\Phi$ is obtained by applying cylindrical coordinates $(\rho \cos \varphi, \rho \sin \varphi, z)$ except z-dependence on the Laplace equation as follows form;

$$\mathbf{E}_1 = E_0 \frac{2\epsilon_2}{\epsilon_1 + \epsilon_2} \mathbf{n}_x, \quad (2.34)$$

$$\mathbf{E}_2 = E_0 \mathbf{n}_x + E_0 \frac{\epsilon_1 - \epsilon_2}{\epsilon_1 + \epsilon_2} \frac{a^2}{\rho^2} (1 - 2 \sin^2 \varphi) \mathbf{n}_x + 2E_0 \frac{\epsilon_1 - \epsilon_2}{\epsilon_1 + \epsilon_2} \frac{a^2}{\rho^2} \sin \varphi \cos \varphi \mathbf{n}_y, \quad (2.35)$$

where ϵ_1 and ϵ_2 are the complex dielectric constants of the wire and the medium, respectively. If the frequency dependence of ϵ_2 is neglected, ϵ_2 can be considered as constant by this assumption, the fields diverge in the case of $\text{Re}(\epsilon_1(\lambda)) = -\epsilon_2$. This case is satisfied if the $\text{Im}(\epsilon_1(\lambda))$ is small at that wavelength [29], [21]. These

conditions reveal LSPR of the wire that shifts with respect to the changes in the ϵ_2 and takes shape based on ϵ_1 .

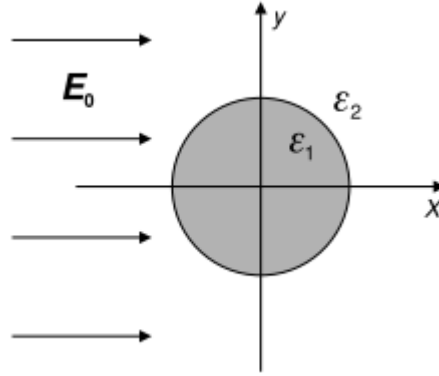


Figure 2.9: Schematic diagram of cross section of a wire and x -polarized plane wave [21].

In the case of a spherical particle with radius a , the solution of the electric field $\mathbf{E} = -\nabla\Phi$ that is determined by applying incident electric field along the x -direction and using spherical coordinates (r, θ, φ) is as follows:

$$\mathbf{E}_1 = E_0 \frac{3\epsilon_2}{\epsilon_1 + 2\epsilon_2} (\cos \theta \mathbf{n}_r - \sin \theta \mathbf{n}_\theta) = E_0 \frac{3\epsilon_2}{\epsilon_1 + 2\epsilon_2} \mathbf{n}_x, \quad (2.36)$$

$$\mathbf{E}_2 = E_0 (\cos \theta \mathbf{n}_r - \sin \theta \mathbf{n}_\theta) + \frac{\epsilon_1 - \epsilon_2}{\epsilon_1 + \epsilon_2} \frac{a^3}{r^3} E_0 (2 \cos \theta \mathbf{n}_r + \sin \theta \mathbf{n}_\theta). \quad (2.37)$$

In this case resonance condition is satisfied when $\text{Re}(\epsilon_1(\lambda)) = -2\epsilon_2$ that causes the field is enhanced relative to the incident field. Furthermore, resonance condition is limited according to the value of the $\text{Im}(\epsilon_1(\lambda))$ [21], [29].

Electrostatic approximation does not present size dependent results due to the complicated calculations necessary to solve the Maxwell's equations. However, LSPR is sensitive to the size of the metallic nanostructures. When the particle size increases, multipolar resonances (especially quadrupole plasmon resonances) are considered. In this case, dipole plasmon resonance shifts to the red and new quadrupole resonance peak arises at a different wavelength [29], [34].

It can also be concluded that localization of the field near the surface for the particle is stronger than that of the wire. It is also important to note that the external field \mathbf{E}_0

induces the dipole $\boldsymbol{\mu} = \varepsilon_2 \alpha(\omega) \mathbf{E}_0$, where $\alpha(\omega)$ corresponds to the polarizability, that is at the center of the sphere and electrostatic field of this dipole is equivalent to the second term of the \mathbf{E}_2 . Aforementioned polarizability is expressed as:

$$\alpha(\omega) = 4\pi\varepsilon_0 a^3 \frac{\varepsilon_1(\omega) - \varepsilon_2}{\varepsilon_1(\omega) + 2\varepsilon_2} \quad (2.38)$$

Absorption and scattering cross sections are in the following forms:

$$\sigma_{abs} = \frac{k}{\varepsilon_0} \text{Im}[\alpha(\omega)] \quad (2.39)$$

$$\sigma_{scatt} = \frac{k^4}{6\pi\varepsilon_0^2} |\alpha(\omega)|^2 \quad (2.40)$$

where k is the wavevector in the medium. Absorption cross section depends on third power of radius of the particle while scattering cross section depends on sixth power of it. It is obvious that absorption is dominated for the small particles whereas scattering is dominated for large particles [21].

Ag NPs has a strong extinction (absorption + scattering) that corresponds to the LSP band as shown in Figure 2.10 according to the UV-Visible spectrophotometry measurements.

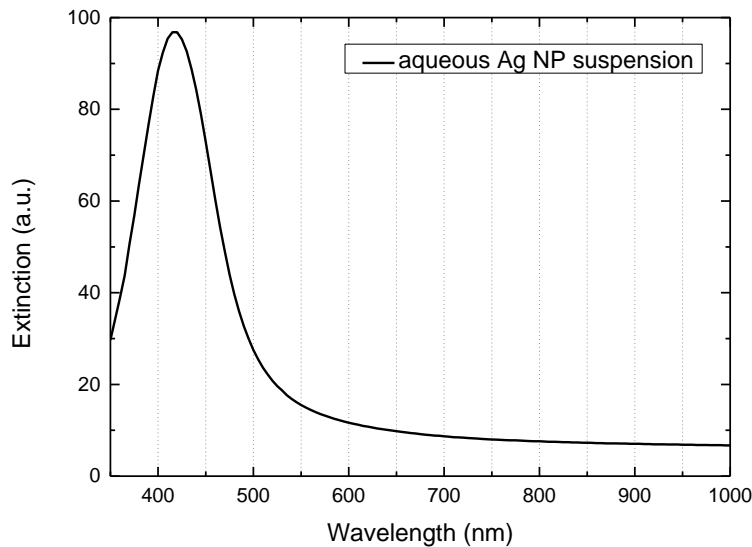


Figure 2.10: UV-Vis extinction spectrum of colloidal Ag NPs in water.

This peak is obtained in the case of frequency resonance between the incident field and oscillating electrons in nanoparticle. Increase in the size of nanoparticles causes this peak shift to the higher wavelengths [35].

In the extinction spectra of the Ag NWs, two or more peaks are exhibited in the UV region through lack of cross-section symmetry [36]. Colloidal Ag NWs rule out to obtain extinction spectrum in the NIR region. In Figure 2.11, extinction spectrum of Ag NWs that are coated on pet substrate by spray coating is presented. Transverse oscillations of electrons are represented in visible region of the spectrum with a peak corresponds to the SPR mode and shoulder of it represents the shape dependent resonance peak [35]. However, length/wide aspect ratio of Ag NWs is very high and longitudinal mode peak does not observed in NIR region of the spectrum.

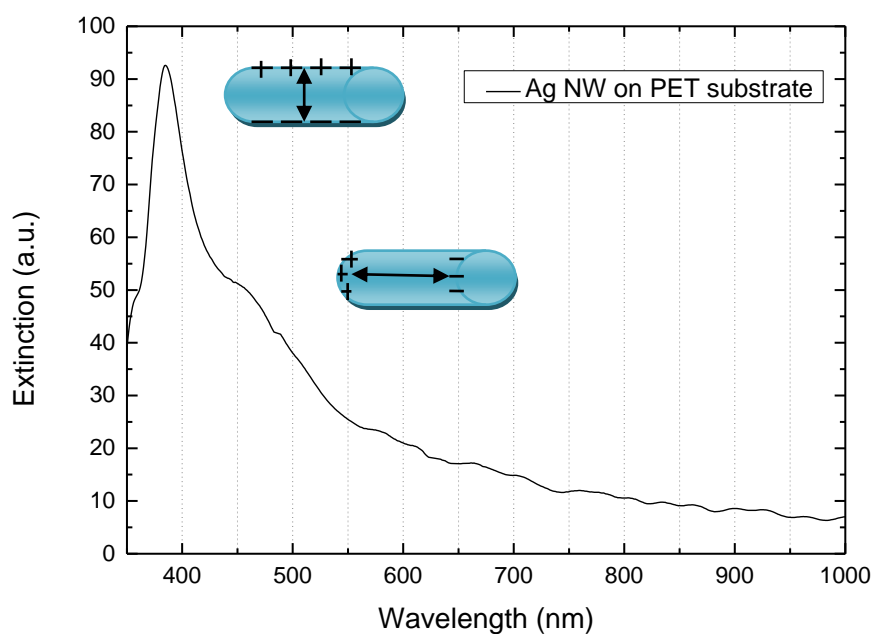


Figure 2.11: UV-Vis extinction spectrum of spray coated Ag NWs on pet substrate and schematic representation of transverse (at shorter wavelengths) mode for Ag NW and longitudinal (at higher wavelengths) surface plasmon mode for Ag nanorods.

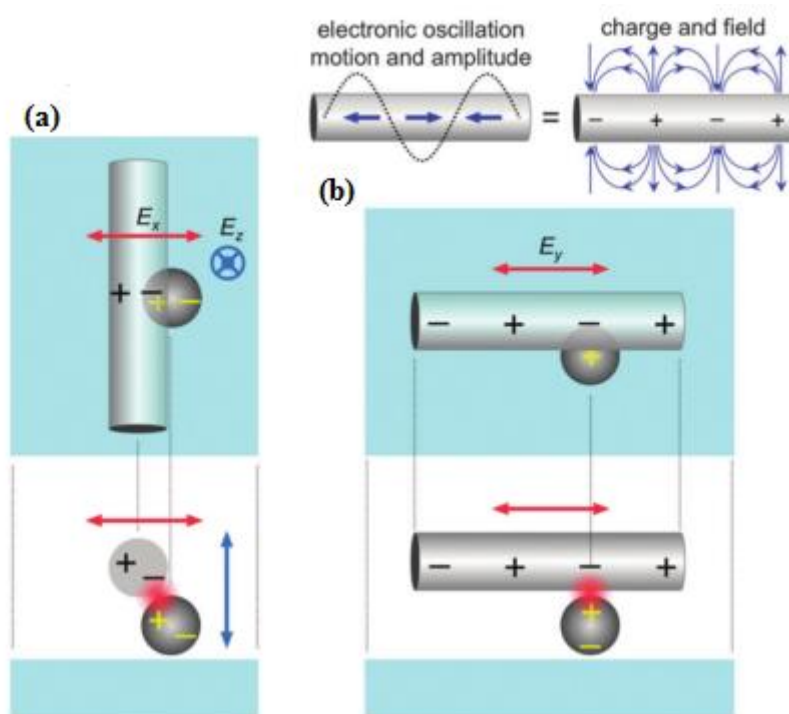


Figure 2.12: Schematic representation of transverse (a) and longitudinal (b) plasmon modes of a nanowire and dipolar plasmon mode of a nanosphere corresponding to the x- and y- polarized incoming light [37].

In Figure 2.12, coupling between plasmon modes of a nanowire and a nanosphere is illustrated [37]. Explanations of factors causing EF of Ag NP and Ag NW are more comprehensive than that of polarization property of the incoming light.

Electromagnetic enhancement is strongly dependent on extinction band or bands of metal nanostructures [38]. EF reaches its maximum value when LSPR is between the Stokes process and incoming light frequency [27], [39], [40].

2.3.2. Chemical Field Enhancement

Chemical enhancement originates from the interaction of the metallic structure and the analyte molecule that is near-field of it and causes change of Raman polarizability tensor [9]. Enhanced Raman signals are proportional to the physical and chemical interactions, orientation of the molecules and charge-transfer theory with a factor up to 10^2 [18]. In most cases, orientations of the molecules according to the incident beam polarization are random. Some proposals for charge transfer theory can be

summarized as the non existence of covalent bond between the adsorbate and the metal resulting in the change of the electronic distribution of the adsorbate or existence of covalent bond between the adsorbate and the metal resulting in the change of polarizability of the molecule [9]. In addition, Raman cross sections for non-resonant conditions ca. $10^{-30} - 10^{-25}$ cm²/molecule for used scatterer molecule. Larger cross sections as high as 10^{-16} cm²/molecule relating to EF of about 10^{14} are obtained due to the electronic interactions between adsorbate and metal and provides single molecule to be detected [1], [16].

2.4. Enhancement Factor

Enhancement factor (EF) results from the sum of the contributions from the chemical and the electromagnetic enhancement. It depends on the shape of the nanostructures, gaps between aggregated nanostructures, polarization and LSPR wavelength [16], [23].

When a nanoparticle is illuminated by a plane wave under resonant condition, electric field lines concentrates near the nanoparticle as shown in Figure 2.13 [41]. Hence, effective cross section of nanoparticle increases and LSPR modes becomes very impressive for molecule detection and investigation of the plasmonics.

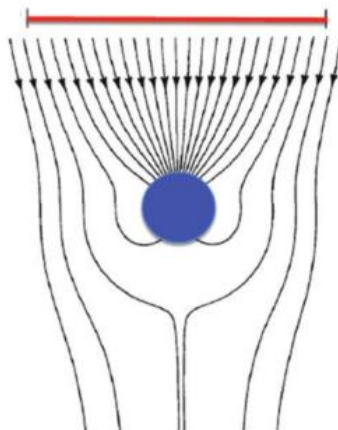


Figure 2.13: Schematic representation of increase in cross section of a nanoparticle under resonant condition [41].

Maximum value of EF is reached through molecules located in the regions, called as hot spots, between two or more metal nanostructures that are coupled in the near

field [29]. In Figure 2.14, a molecule (BCB) located between two Ag NPs is represented.

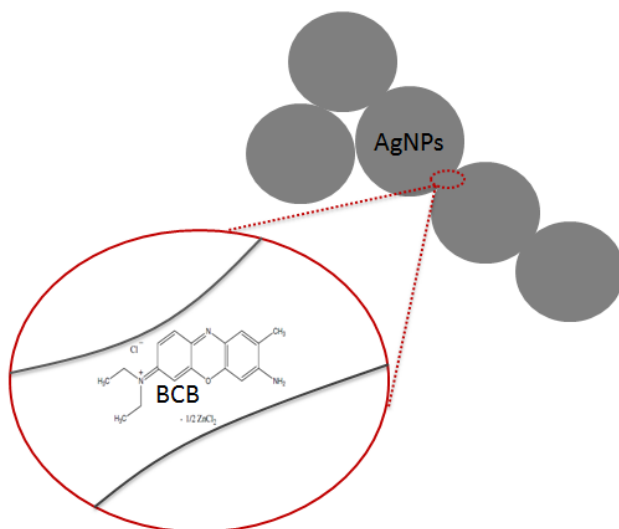


Figure 2.14: Schematic representation of a molecule (BCB) between hot spot of two Ag NPs.

Edges of the cross-sections and ends of the Ag NWs are expected to be the maximum EF resources [36].

In addition, because the surfaces of polyol synthesized Ag NP and Ag NWs are smooth crystalline at atomic level, their plasmon lifetimes are longer when coupling of these nanostructures are considered. This phenomenon was modeled in a research by revealing second harmonic generation properties using two metal nanostructures. It was concluded that enhancement of second harmonic signal is acquired compared to the non-coupled nanostructures [42].

EF is defined as in the following form:

$$EF_{\text{SERS}}(w_v) = \frac{|E_{out}(w)|^2 |E_{out}(w-w_v)|^2}{E_0^4} \quad (2.41)$$

where $E_{out}(w)$ and $E_{out}(w - w_v)$ correspond to the incoming light and Stokes-shifted Raman, respectively. Raman peaks are observed in the $100\text{-}3000\text{ cm}^{-1}$ interval by virtue of small difference between the energy of these fields [23]. Hence,

difference between $E_{out}(w - w_v)$ and $E_{out}(w)$ can be neglected by approximation and more applicable relation at a desired point is obtained [33]:

$$EF_{SERS} = \frac{|E(r)|^4}{|E_0(r)|^4} \quad (2.42)$$

This expression is used to compare the experimental and theoretical results [29], and does not involve the affect of the chemical contributions.

E. C. Le Ru at all. [43] classified the possible EF calculation methods as the single molecule EF, the analytical chemistry point of view and the SERS substrate point of view.

Single molecule enhancement factor is calculated as follows:

$$SMEF = \frac{I_{SERS}^{SM}}{\langle I_{RS}^{SM} \rangle} \quad (2.43)$$

where I_{SERS}^{SM} and $\langle I_{RS}^{SM} \rangle$ correspond to the single molecule SERS intensity and the average Raman intensity per molecule.

Analytical enhancement factor is calculated by:

$$AEF = \frac{I_{SERS}/c_{SERS}}{I_{RS}/c_{RS}} \quad (2.44)$$

where I_{SERS} and I_{NRS} correspond to the SERS and NRS intensities, respectively. c_{SERS} and c_{RS} are concentration of molecules in SERS and Raman conditions, respectively [43].

In SERS substrate point of view, EF of surface averaged structures is established by calculating the ratio of SERS to normal Raman scattering (NRS) of analyte molecule in the following form:

$$EF = \frac{I_{SERS}/N_{SERS}}{I_{NRS}/N_{NRS}} \quad (2.45)$$

where I_{SERS} and I_{NRS} represent SERS and NRS intensities in unit of $[\text{cts mW}^{-1}\text{s}^{-1}]$, respectively, and N_{SERS} is the total number of molecules adsorbed on metal nanostructures. N_{NRS} is defined as:

$$N_{\text{NRS}} = C_{\text{NRS}} V_{\text{probe}} \quad (2.46)$$

where C_{NRS} is the total number of molecules per mL and V_{probe} corresponds to the probe volume for Raman scattering [44].

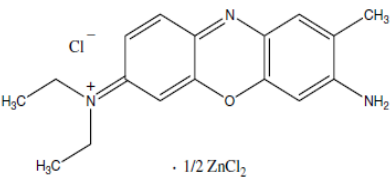
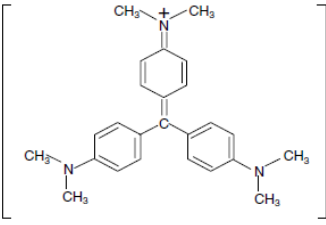
CHAPTER 3

EXPERIMENTAL TECHNIQUES

3.1. Synthesis

10^{-4} , 10^{-5} and 10^{-6} M brilliant cresyl blue (BCB) and crystal violet (CV) dye molecules were used for the Raman scattering measurements. A few properties of these molecules are provided in table 3.1. Colloidal Ag NPs and Ag NWs were used to enhance the Raman signal.

Table 3.1: Molecular structure of the dye molecules and their physical characteristics [45].

Molecular Structure	 <p style="text-align: center;">BCB</p>	 <p style="text-align: center;">CV</p>
CA Index Name	Phenoxazin-5-ium, 3-amino-7-(diethylamino)-2-methyl-, chlorozincate (2:1)	Methanaminium, N-[4-[bis[4-(dimethylamino)phenyl]methylene]-2,5-cyclohexadien-1-ylidene]-N-methyl-, chloride (1:1)
Chemical/Dye Class	Phenoxazine	Triphenylmethane
Molecular Formula	$C_{17}H_{20}ClN_3O \cdot 0.5 ZnCl_2$	$C_{25}H_{30}ClN_3$
Molecular Weight	385.96	407.98
Absorption (λ_{max})	622 nm	590 nm

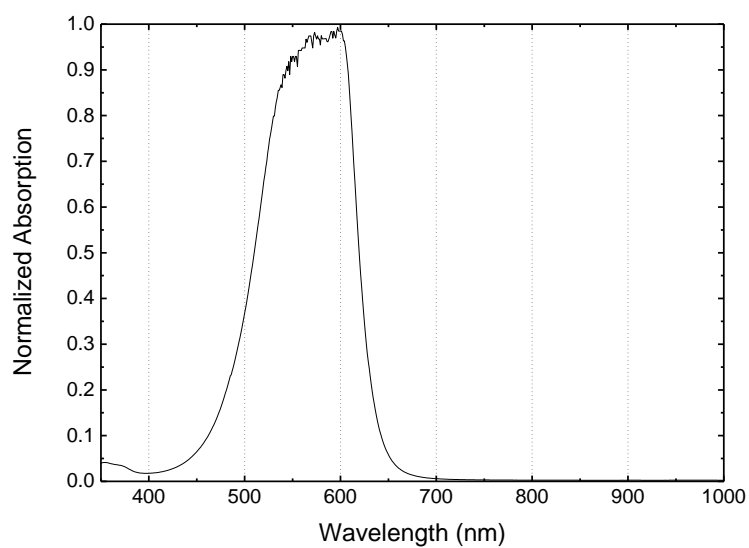


Figure 3.1: UV-Visible absorption spectrum of CV solution.

Absorption maximum wavelength of CV solution corresponds to 590 nm according to the UV-Visible spectrophotometry measurements as shown in Figure 3.1.

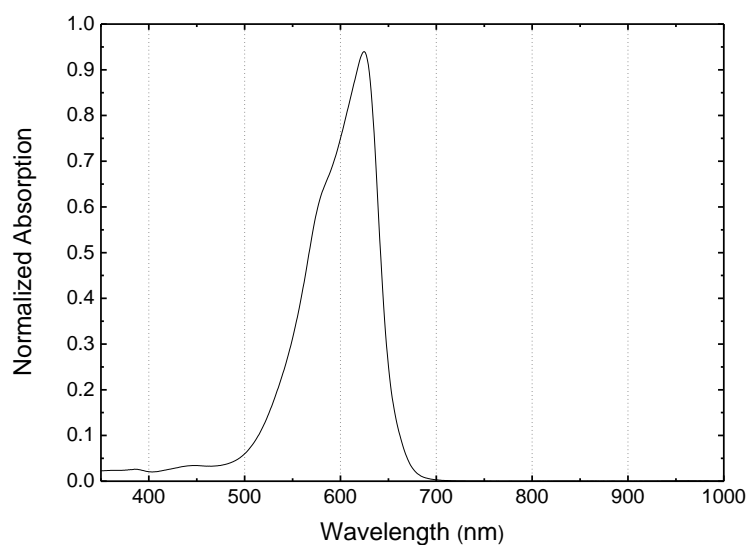


Figure 3.2: UV-Visible absorption spectrum of BCB solution.

Absorption maximum wavelength of BCB solution corresponds to 622 nm as shown in Figure 3.2.

Enhancement of Raman signal was acquired by adsorption of BCB and CV molecules efficiently on the nanostructures. BCB and CV are soluble in water in

addition to the other liquids. Both of them are used in staining, biological and industrial applications [45].

3.1.1. Polyol Synthesis of Ag NPs

100 mL round bottom flask was cleaned by deionized water, acetone and isopropyl alcohol. 10 mL ethylene glycol (EG) solution of polyvinylpyrrolidone (PVP) was poured into the beaker. 500 mg sodium chloride (NaCl) and a magnet were added into the EG solution. Parafilm was placed over the beaker. The solution was heated at 80 °C and stirred at a rate of 1000 rpm at a hot plate with magnetic stirrer and waited until the dissolution of the PVP. After that, the solution was placed into the silicon oil bath to be heated and stirred at 1000 rpm at the same time. This step was conducted by the help of a hot plate with magnetic stirrer which is placed under the distillation set up. While the first solution was heated and stirred, 10 mL of EG solution and 200 mg silver nitrate (AgNO_3) were added into a cleaned beaker. This solution was stirred at 1000 rpm by a magnetic stirrer. Following dissolution, it was added dropwise into the PVP solution by an injection pump (Top-5300 model syringe pump) at a rate of 5 mL/h. Until the end of the synthesis, PVP solution was heated and stirred. Upon cooling to room temperature, the solution was diluted with acetone and centrifuged two times at 7000 rpm for 20 minutes. Nanoparticles were then collected and dispersed in ethanol [46].

3.1.2. Polyol Synthesis of Ag NWs

Glassware were cleaned with deionized water, basic and acidic solutions, acetone, isopropyl alcohol, and deionized water. 7 mg of NaCl was added into the 10 mL of 0.45 M EG solution of PVP. This solution was heated at 170 °C. At the same time, 0.12 M AgNO_3 was added into the 5 mL of EG and distilled into the PVP solution by an injection pump at a rate of 5 mL/h. This solution was stirred at 1000 rpm until the end of the distillation process. By the addition of Ag^+ ions into the solution, Ag NPs form in the nanometer scale due to the adsorption of PVP molecules onto these structures. Larger Ag NPs form after some of the Ag NPs begin to dissolve through Oswald ripening. Multitwin particle formation is another possibility due to the fact

that PVP passivates some facets of these particles. Passivation of (100) faces of formed multitwin particles and actively released (111) planes for the anisotropic growth at [110] direction allowing the multitwin particles to become Ag NWs. Once the distillation process is complete, solution was annealed at 170 °C for 30 minutes, and then cooled to room temperature. Ag NWs were purified by acetone at a ratio of 1:5 and centrifuged at a rate of 7000 rpm for 20 minutes. Then, the Ag NWs were dispersed in ethanol for further use [46].

3.2. Substrate Preparation

Steps in substrate preparation are illustrated in Figure 3.3. N-type, 1-3 ohm-cm single side polished silicon wafers that are 500 μm thick were cut by diamond point pencil in 1 cm 1 cm dimensions. They were cleaned with acetone, isopropyl alcohol, and deionized water for 15 minutes, respectively, in an ultrasonic bath and dried under nitrogen flow. To conduct the reference measurements for Raman scattering, a drop of CV solution on a Si wafer was prepared. Three types of substrates were prepared for the measurement of the SERS effect and these were:

1. CV/BCB solution drop casting on Si wafer for reference Raman measurements;
2. Spray Coating of Colloidal Ag NP/Ag NW and Spin Coating of CV and BCB on Si wafer;
3. Spray coating of in-solution mixed Ag NPs + CV/BCB on Si wafer.

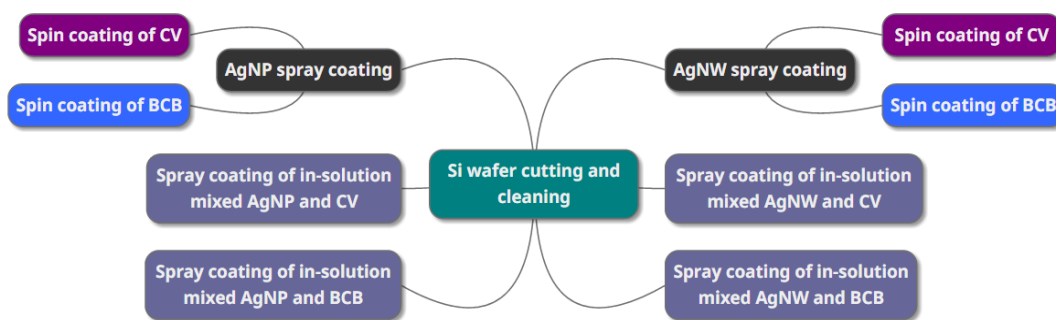


Figure 3.3: Concept map illustrating the substrate preparation steps.

Wafers were stuck by tape onto a hot plate at 80 °C to evaporate ethanol in colloidal Ag NPs/Ag NWs. Spray coating was performed to deposit colloidal Ag NPs/Ag

NWs to wafers. It is crucial to keep the same distance between spray nozzle and wafers during spray coating to obtain highly structured and reproducible surfaces. Number of pass was conducted after about 20 seconds to enable evaporation of ethanol. Surfaces were spray coated by 20, 30 and 40 number of passes for each different molarities of dye molecules. The spray coated wafers were dried overnight at room temperature. Depositions of dye molecules onto spray coated surfaces were conducted via spin coating (Speciality Coating Systems Spincoat G3-8). A 600 μl of dye molecule was dropped onto to the Ag NP/Ag NW spray coated wafers to cover the surface as shown in Figure 3.4. After some tries to optimize the spread of the dye molecules, 5 seconds of acceleration time, 30 seconds of spin time, 2000 rpm of spin speed and 3 seconds of deceleration time were adjusted.

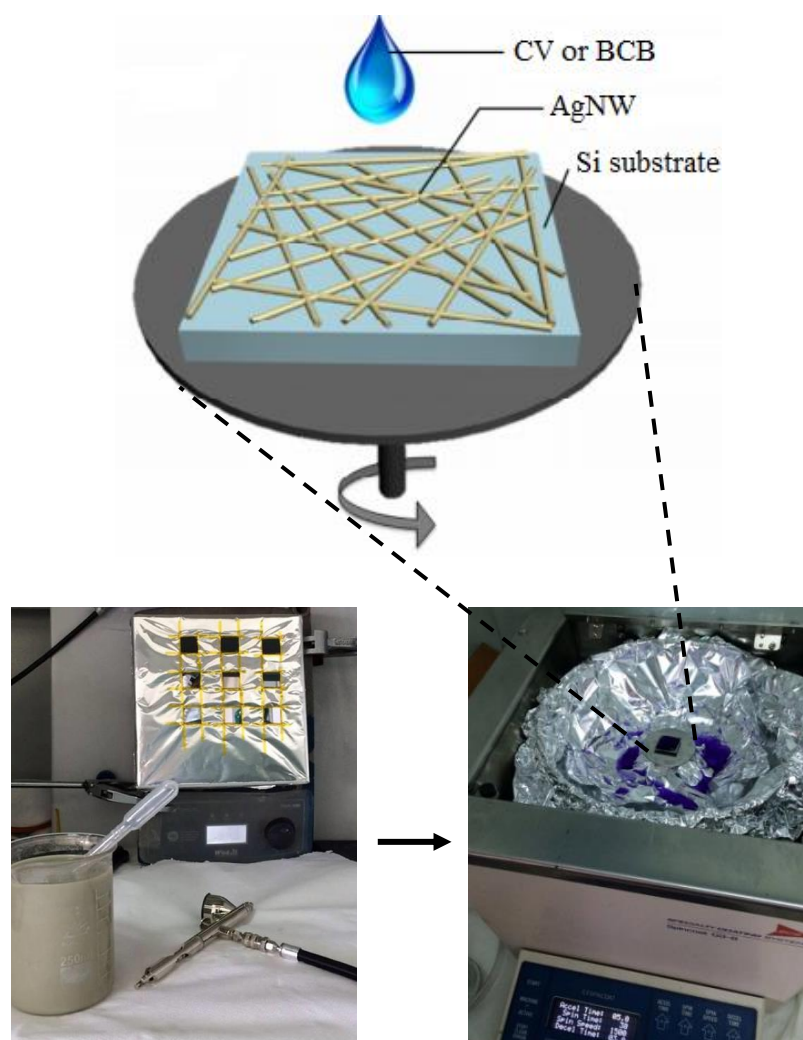


Figure 3.4: Experimental setup for spin coating of CV or BCB after spray coating of Ag NW on Si substrates [47].

Wafers were also coated by in-solution mixed Ag NPs/Ag NWs and CV/BCB. The ratio of colloidal Ag NP/Ag NW and dye molecules which were mixed was five to three. The process of preparation of the wafers and spray coating was same as the previous spray coating step.

3.3. Characterization

Prepared samples were characterized by Scanning Electron Microscope to evaluate the surface coverage, reflection setup to obtain total and diffuse reflection spectra and Raman spectroscopy to obtain normal Raman and SERS spectra.

3.3.1. SEM Analysis

Scanning electron microscope (SEM) was operated at 20 kV for substrates prepared by spray coating of Ag NP and one image of all samples was acquired with magnification of 5000 that represents the general surface coverage of the samples. SEM images of different locations of these representative images were obtained with magnification of 20000 in order to calculate surface coverage values. For substrates prepared by spray coating of Ag NW, representative images were obtained with magnification of 2000 and in order to calculate the surface coverage values of different locations of these images, magnification of 10000 was adjusted.

3.3.2. Raman Measurements

Raman measurements were carried out by the experimental set-up represented in the Figure 3.5. Sample was illuminated by an illumination source via integrated camera inside the Raman head. 532 nm radiation with frequency doubled DPSS Nd-YAG SLM laser (Laser Quantum torus) at power of 0.32 mW was transferred to the Raman head through optical fiber cable. This transferred light was focused onto the sample. 50 μm diameter focal spot size was acquired by a fiber coupled measurement head with 50X objective lens. Rayleigh scattered photons were blocked by a band gap filter that is at the exhaust port of the Raman head. Shorter wavelengths that are shorter than 532 nm are also blocked to protect the CCD camera. Inelastically scattered photons are collected by the Raman head and sent to the spectrometer with another optical fiber cable. A f/6.4 550 mm Raman spectrometer (Horiba Jobin-Yvon iHR550) with a 1024x256 pixel CCD (Horiba Synapse) was used to diffract the

collected light by a grating and dispersed to separate the wavelengths of it on the CCD chip. The acquisitions were performed with 98 μm slit width and 600 grooves/mm blazed grating at 500 nm. Collected data was sent to the computer by CCD camera and labspec software was used to analyze it.

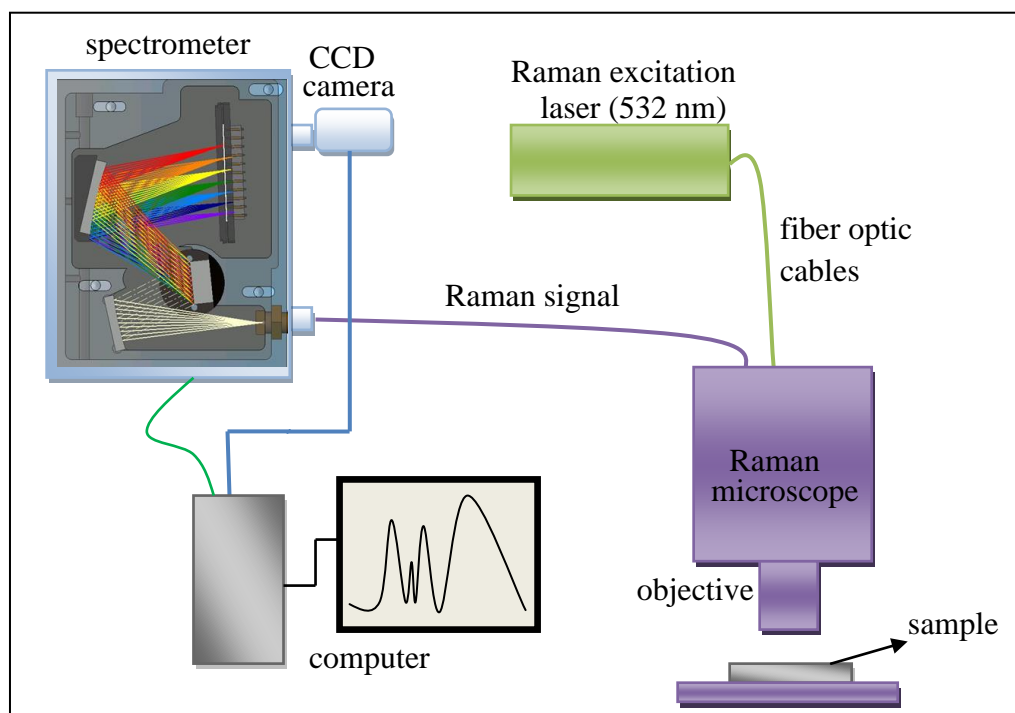


Figure 3.5: Schematic diagram of the Raman setup.

3.3.3. Reflection Measurements

Total reflection and diffuse reflection measurements were carried out by reflection set-up illustrated in Figure 3.6. Light was focused on the almost closed diaphragm by a condenser lens. After the beam passed through the diaphragm, it was chopped at the chopper and sent to the focusing lens to be collimated. The image of the diaphragm opening was obtained as a spot on the reflection (R) port of the integrating sphere. To measure the total reflection, dark background measurement was carried out by leaving the R and transmission (T) ports empty, then reference measurement was carried out by putting BaSO₄ calibration disk at R port. Finally, sample was placed at the R port and T port was left empty. To measure the diffuse reflection, specular R port was opened and same steps in reflection measurements were repeated. The collected light was sent to the monochromator and detector.

Furthermore, a reflectance dataset (R_{BaSO_4}) was used for reflectance calculations because the total reflection of the owned $BaSO_4$ is below 100% [48], [49].

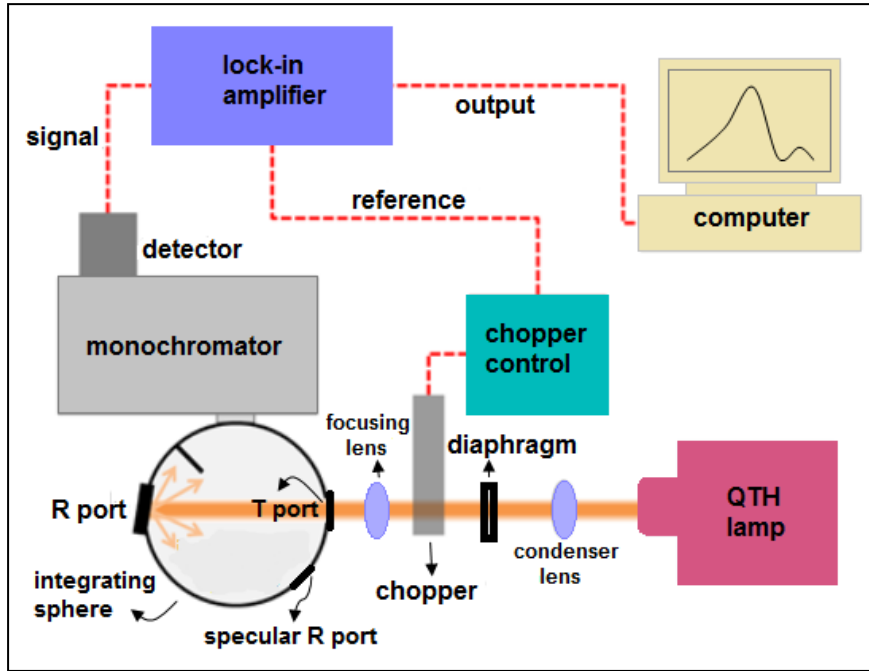


Figure 3.6: Schematic diagram of the reflection measurement set-up [50].

Total reflection and diffuse reflection are calculated through the following relations:

$$\text{Total Reflection} = \frac{R - \text{Dark}}{(\text{Ref}/R_{BaSO_4}) - \text{Dark}} \quad (3.1)$$

$$\text{Diffuse Reflection} = \frac{R^* - \text{Dark}^*}{(\text{Ref}^*/R_{BaSO_4}) - \text{Dark}^*} \quad (3.2)$$

where Dark and Ref correspond to the signals that are obtained from dark background measurement and reference measurement, respectively. Dark* and Ref* correspond to the signals that are obtained by same measurements but by opening specular R port. In addition, haze is defined as follows:

$$\text{Haze} = \frac{\text{Diffuse Reflection}}{\text{Total Reflection}} \times 100 \quad (3.3)$$

CHAPTER 4

RESULTS and DISCUSSION

4.1. SEM Images and Reflection Results for Ag NPs

Analysis of SEM images was performed by using a software program named Gwyddion. This analysis enabled number of grains, mean grain size and surface coverage values to be obtained. Samples prepared with 10^{-4} M CV and BCB spin coating on Ag NP spray coating were analyzed, and these results were used for the samples prepared with 10^{-5} and 10^{-6} M CV and BCB as the preparation method was the same.

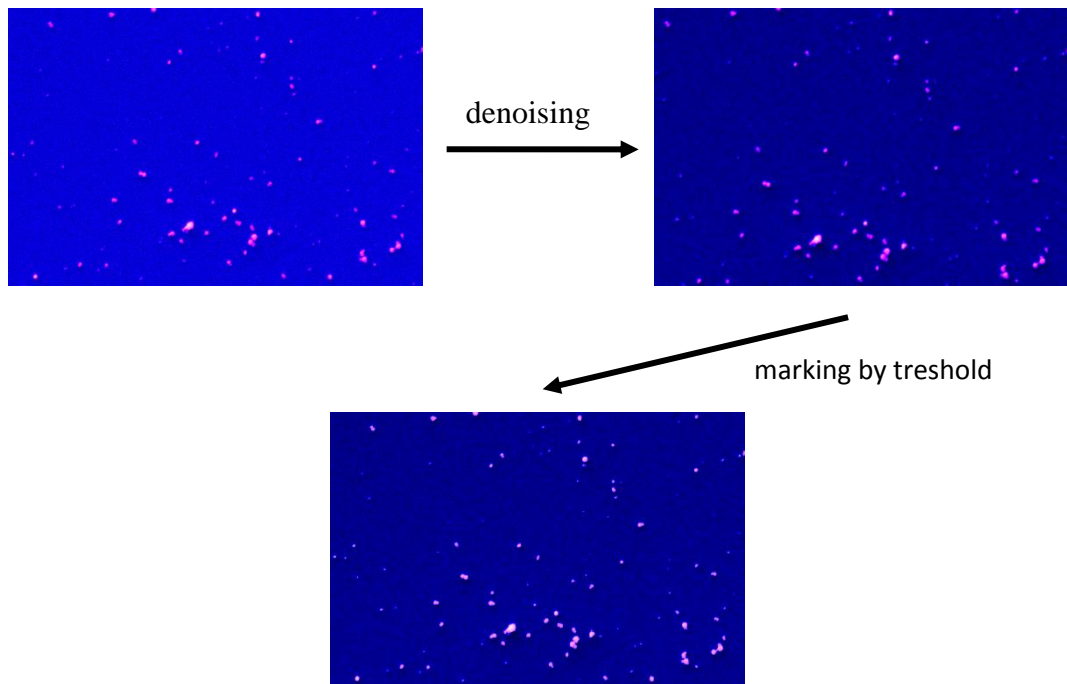


Figure 4.1: Image analysis steps for Ag NP SEM images showing application of denoise filter and marking Ag NPs by threshold.

This analysis procedure was also applied for samples that were prepared by 10^{-4} M CV and BCB spin coating on Ag NW spray coating, and in-solution mixed Ag NPs/Ag NWs + 10^{-4} M CV/BCB. The same analysis steps were applied for all images. Denoise filter was applied to reduce the noise, and grains were marked by threshold with the proper height and slope percentages as shown in Figure 4.1.

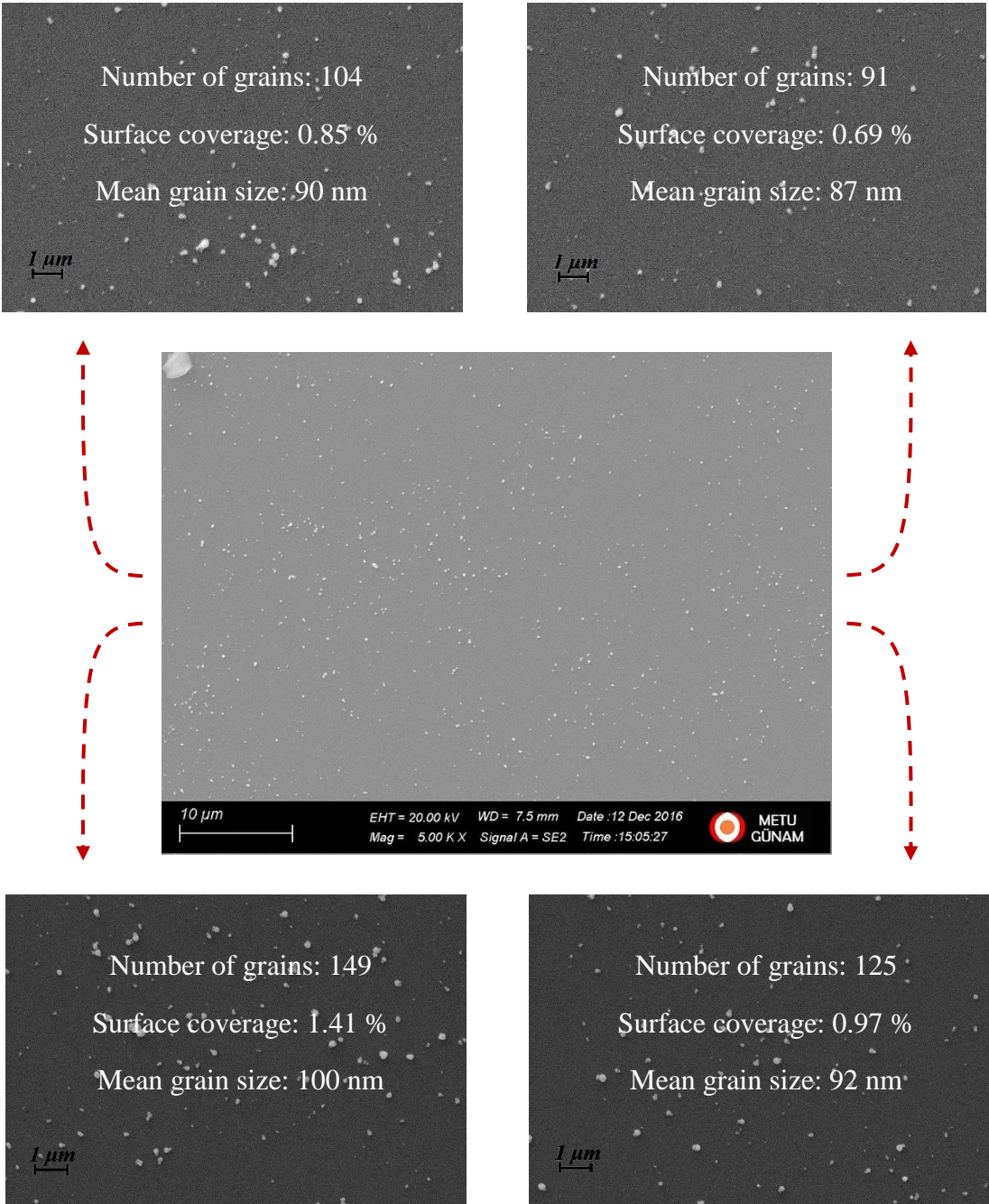


Figure 4.2: SEM image of 10^{-4} M BCB spin coating on Ag NP spray coating with 20 times pass (middle) and images taken from 4 different locations of it.

Then, statistics of grains were acquired. In Figure 4.2, SEM image of Ag NP spray coating with 20 times pass is presented in the middle and other 4 images that were measured by focusing on the 4 different locations of this image for image analysis is presented. Number of Ag NPs, surface coverage and mean Ag NP size were obtained by image analysis steps.

Table 4.1: Surface coverage values of Ag NPs for different substrate preparation techniques and 20, 30 and 40 times pass of Ag NP.

	<i>Ag NP spray coating and CV spin coating</i>	<i>spray coating of in-solution mixed Ag NPs and CV</i>	<i>Ag NP spray coating and BCB spin coating</i>	<i>spray coating of in-solution mixed Ag NPs and BCB</i>
20 times pass	0.5	0.6	1.0	0.7
30 times pass	0.9	2.2	1.2	1.4
40 times pass	1.1	2.6	1.4	1.5

Average of the mean grain size for all SEM images of Ag NPs was determined as 100 nm. In table 4.1, surface coverage values corresponding to the different number of passes for substrates that are prepared with different methods are presented.

Total and diffuse reflection measurements were conducted for a bare silicon wafer to be used as reference data and for the substrates prepared by spray coating of in-solution mixed Ag NPs + 10^{-4} M CV for 20, 30 and 40 times pass numbers correspond to 0.6 %, 2.2 %, and 2.6 % surface coverage values. Total reflection measurements indicate that as the surface coverage increases, total reflection decreases as shown in Figure 4.3 (a). Diffuse reflection measurements indicate inverse relationship as compared to the total reflection measurements as presented in Figure 4.3 (b).

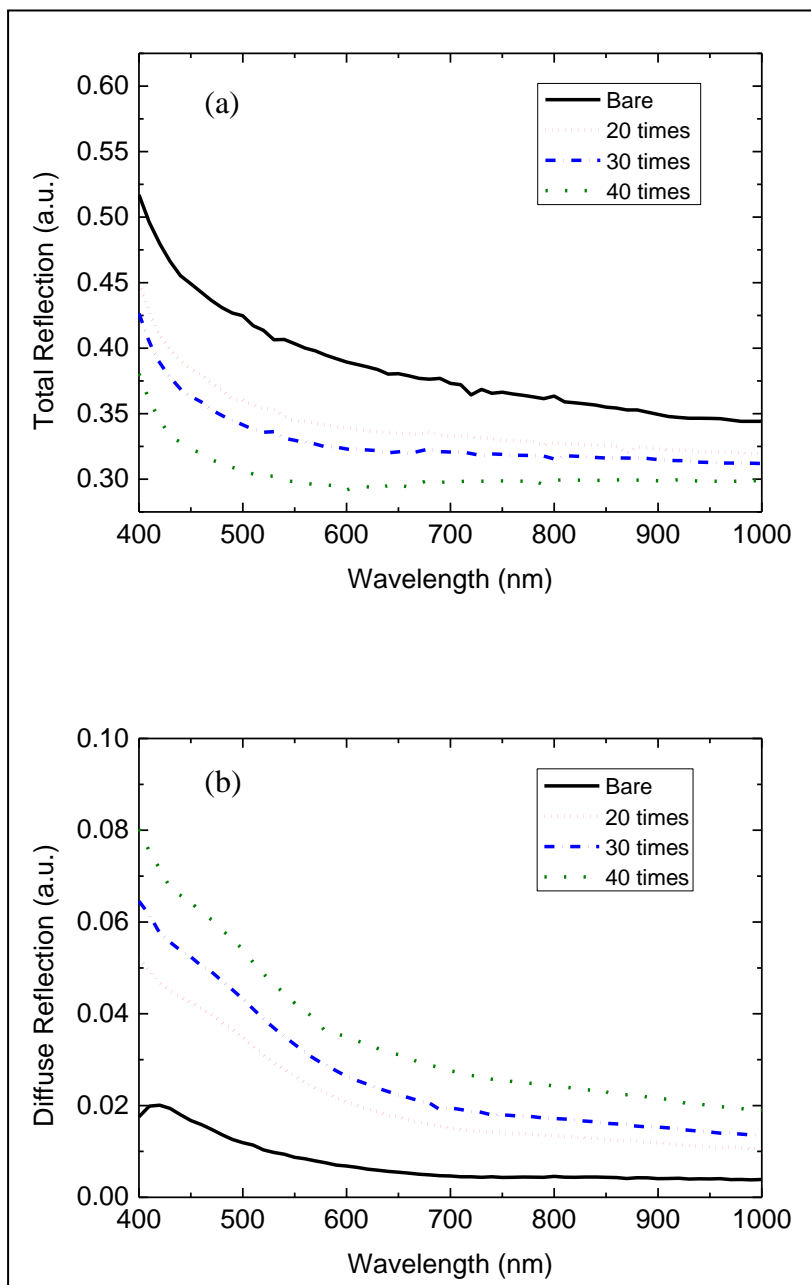


Figure 4.3: Total and diffuse reflection spectra of spray coating of in-solution mixed Ag NPs + 10^{-4} M CV for different number of passes.

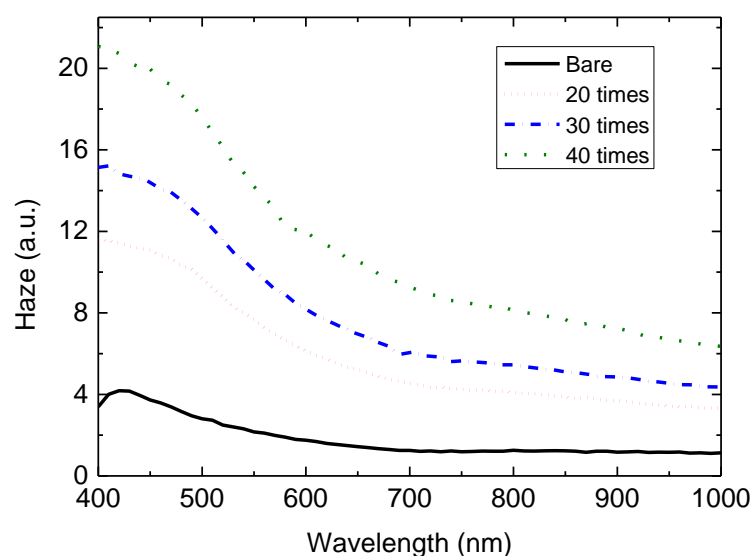


Figure 4.4: Haze spectrum of spray coating of in-solution mixed Ag NPs + 10^{-4} M CV for different number of passes.

Haze measurement results indicate that plasmon resonances for Ag NPs are observed around 400 nm as presented in Figure 4.4.

4.2. Reference Raman Measurement

Acquisition time for reference measurements was conducted in 250 seconds. The peak 1614 cm^{-1} corresponds to the in-plane aromatic C-C stretching vibration according to the literature [51]. Therefore, 1616 cm^{-1} as shown in Figure 4.5 was assigned to this vibration and used for EF calculations. Because the characteristic peaks of BCB could not be obtained in Raman measurement of a droplet of BCB solution on Si wafer, this result was used for BCB molecule also by predicting the results would not be affected considerably.

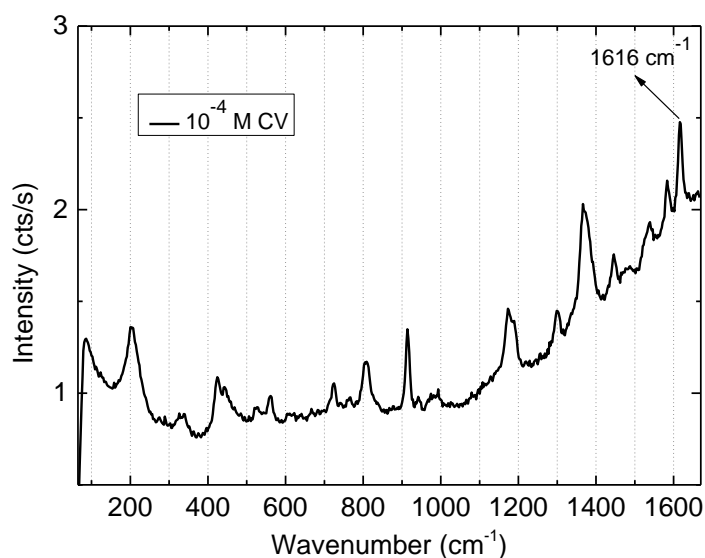


Figure 4.5: Raman spectrum of 10^{-4} M CV liquid droplet on Si wafer.

4.3. SERS Measurements for Ag NPs and CV/BCB

Figure 4.6 shows the normalized extinction spectra of Ag NP and Ag NW, and normalized absorption spectra of CV and BCB.

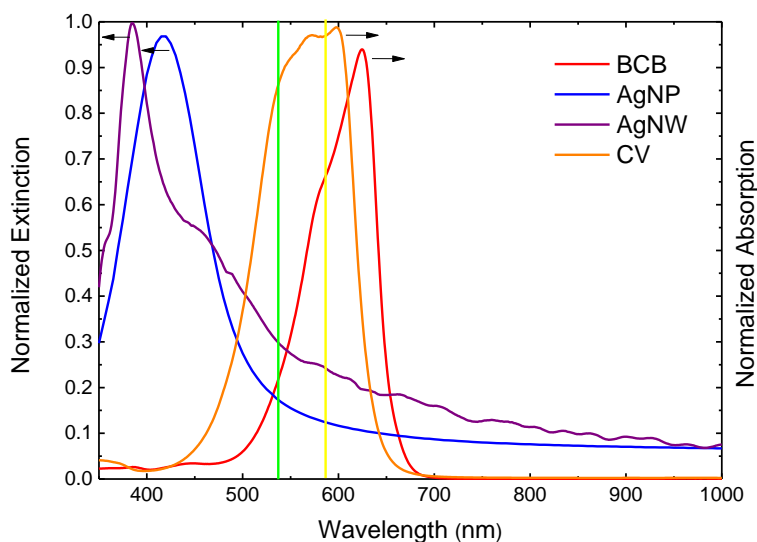


Figure 4.6: Normalized extinction spectra of Ag NP and Ag NW, and normalized absorption spectra of CV and BCB, green line represents the 532 nm laser wavelength and yellow line represents the scattered light wavelength.

According to our experiment conditions, laser wavelength is between the maximum LSPR wavelength of metal nanostructures and absorption wavelength of molecules. This situation was investigated with an analytic model in a recent research [52]. Maximum EF is obtained when LSPR wavelength is between laser light and scattered light wavelength. Hence, more enhancement is expected from Ag NWs due to the fact that some plasmon modes of Ag NW is between the laser light and scattered light wavelength. In addition, laser light is not in resonance with BCB, however wavelength of laser light is close to the CV absorption wavelength maximum. So, expected EF for CV is more as compared to that of BCB.

Acquisition time was set as 250 seconds for samples that had been prepared by spray coating of colloidal Ag NP/Ag NW and spin coating of CV/BCB and spray coating of in-solution mixed Ag NPs and CV/BCB on substrates. SERS measurements were acquired from 10 different selected spots on prepared surfaces. All spectra were normalized for acquisition time.

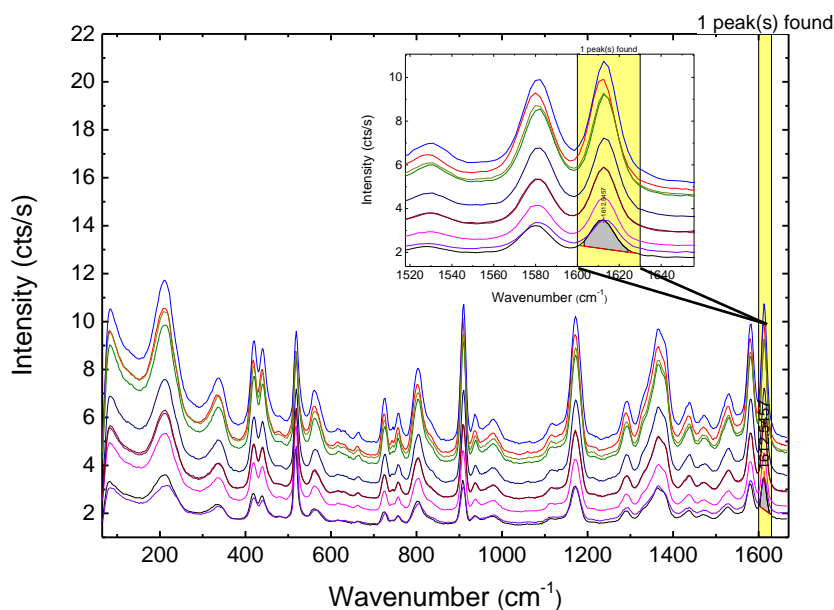


Figure 4.7: SERS intensity spectra of spray coating of in-solution mixed Ag NPs + 10^{-4} M CV with 20 times pass obtained from 10 different selected spots of substrate and peak area under a strong peak between the 1600 and 1630 cm^{-1} to be used for statistics of SERS.

Peak area integrals of the characteristic Raman peaks of CV and BCB were presented in box charts representing the statistics of all measurements. In Figure 4.7, SERS intensity spectra of spray coating of in-solution mixed Ag NPs + 10^{-4} M CV with 20 times pass obtained from 10 different selected spots of substrate is presented. 10 strong peaks between 1600 and 1630 cm^{-1} were baseline corrected and peak areas were obtained from these intensity spectra.

In Figure 4.8, SERS intensity spectra of spray coating of in-solution mixed Ag NPs + 10^{-4} M BCB with 20 times pass obtained from 10 different selected spots of substrate is shown. One of the characteristic peaks of BCB (1419 cm^{-1}) was chosen to calculate EF. 1395 and 1430 cm^{-1} intervals of 10 peaks were baseline corrected and peak areas were obtained.

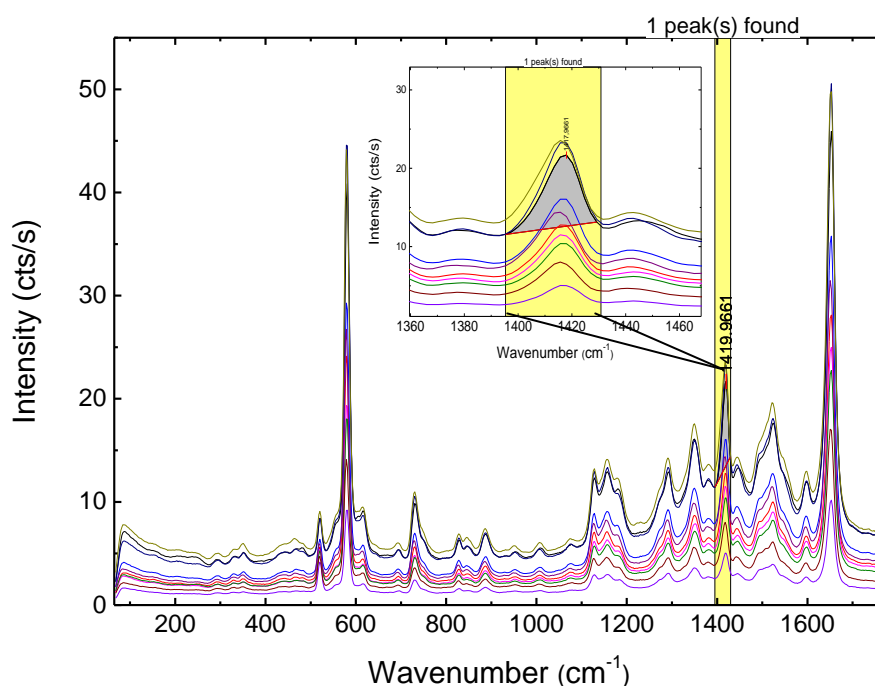


Figure 4.8: SERS intensity spectra of spray coating of in-solution mixed Ag NPs + 10^{-4} M BCB with 20 times pass obtained from 10 different selected spots of substrate and peak area under a strong peak between the 1395 and 1430 cm^{-1} to be used for statistics of SERS.

Calculated peak areas for all substrates prepared with colloidal Ag NPs were used to present the statistics of SERS measurements with box charts that will be shown in the following section.

4.4. Enhancement Factor Calculations and Results for Ag NPs

Area under the peak width between 1600 and 1630 cm^{-1} for CV was found and normalized for laser power in order to use this result as intensity of NRS in EF calculation as follows:

$$I_{NRS} = \frac{5.18}{0.32 \text{ mW s}} \text{ cts} \quad (4.1)$$

In Figure 4.9, schematic representation of Raman measurement from a droplet of 10^{-4} M CV molecule on a Si wafer is shown.

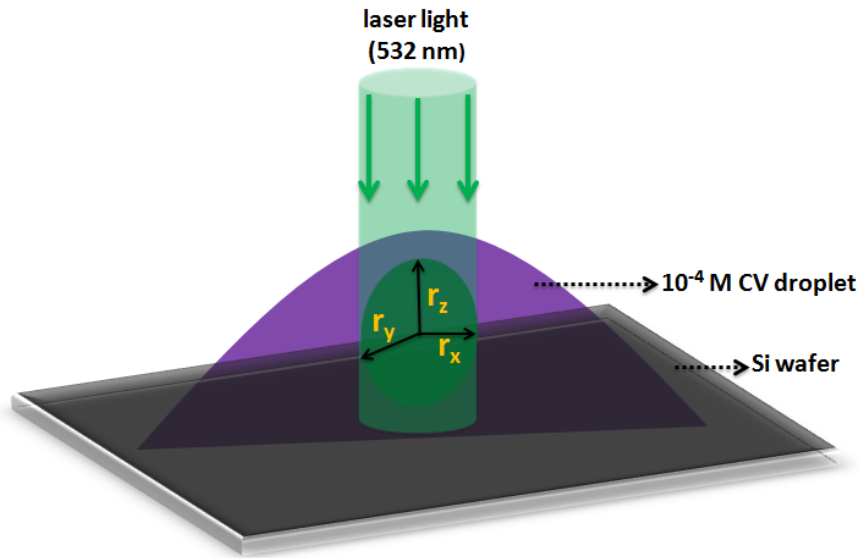


Figure 4.9: Schematic representation of Raman measurement from a droplet of 10^{-4} M CV molecule.

Volume of a prolate spheroid was considered to calculate the probe volume with dimensions of $r_x = 25 \mu\text{m}$, $r_y = 25 \mu\text{m}$ considering the spot size of laser light, and $r_z = 50 \mu\text{m}$ as follows:

$$V_{\text{probe}} = \frac{4\pi}{3} \times 25 \mu\text{m} \times 25 \mu\text{m} \times 50 \mu\text{m} = 1.3 \times 10^{-10} \text{L} \quad (4.2)$$

Total number of molecules in that volume for Raman measurement corresponds to:

$$\begin{aligned}
 N_{\text{NRS}} &= 10^{-4} \frac{\text{mol}}{\text{L}} \times 6.02 \times 10^{23} \frac{\text{molecules}}{\text{mol}} \times 1.3 \times 10^{-10} \text{L} \\
 &= 7.9 \times 10^9 \text{molecules}
 \end{aligned}
 \tag{4.3}$$

In Figure 4.10, SERS measurement of Ag NPs is presented.

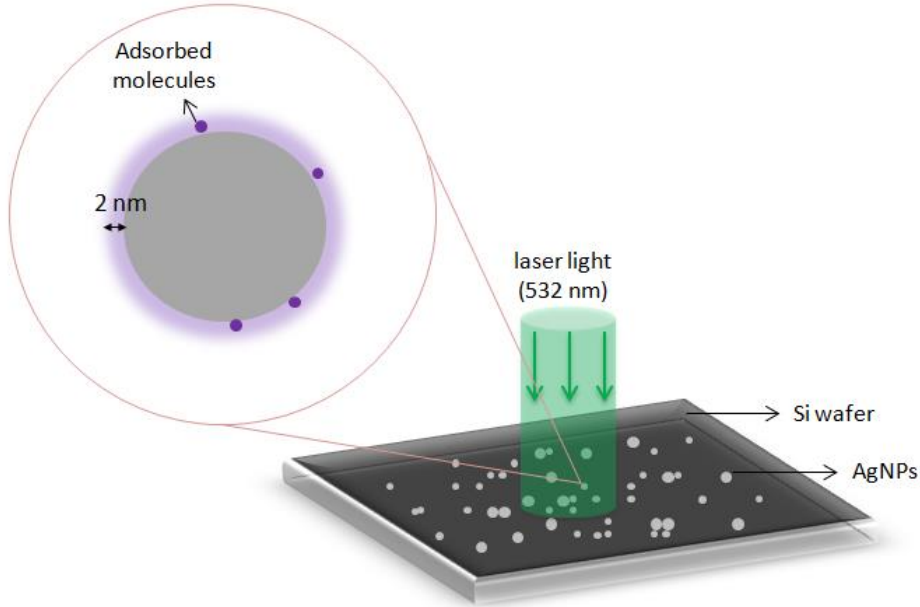


Figure 4.10: Schematic representation of SERS measurement for EF calculation.

SERS EF is acquired from the molecules that exist up to 1-2 nm away from the surface of the metal nanostructure; therefore, this localized volume around one Ag NP that is illustrated in Figure 4.10 was calculated as follows:

$$V_{\text{probe(1Ag NP)}} = \frac{4\pi}{3} \times [(52\text{nm})^3 - (50\text{nm})^3] = 6.5 \times 10^{-20} \text{L}
 \tag{4.4}$$

Total number of 10^{-4} M CV molecules adsorbed on metal nanostructures was calculated by:

$$\begin{aligned}
 N_{\text{SERS}} &= 10^{-4} \frac{\text{mol}}{\text{L}} \times 6.02 \times 10^{23} \frac{\text{molecules}}{\text{mol}} \times 6.5 \times 10^{-20} \text{L} \times 2000 \text{molecules} \\
 &= 3.93 \text{molecules} \times 2000 \text{ molecules} = 7860 \text{ molecules}
 \end{aligned}
 \tag{4.5}$$

Then, EF values for surface averaged structures were acquired by using equations

$$\text{EF} = \frac{I_{\text{SERS}}/N_{\text{SERS}}}{I_{\text{NRS}}/N_{\text{NRS}}} \text{ and } N_{\text{NRS}} = C_{\text{NRS}} V_{\text{probe}}.$$

Before presenting the statistics of SERS measurements, it is beneficial to indicate the corresponding values and ranges in a box chart that is drawn in OriginLab software with a box as shown in Figure 4.11. Half of the data are under the median and half are above it. 75th percentile corresponds to the median of data that is above the median of all the data, whereas 25th percentile is median of data that is below the median of all the data. Hence, 50 percent of the data range is presented in the box and asterisks correspond to the maximum and minimum values.

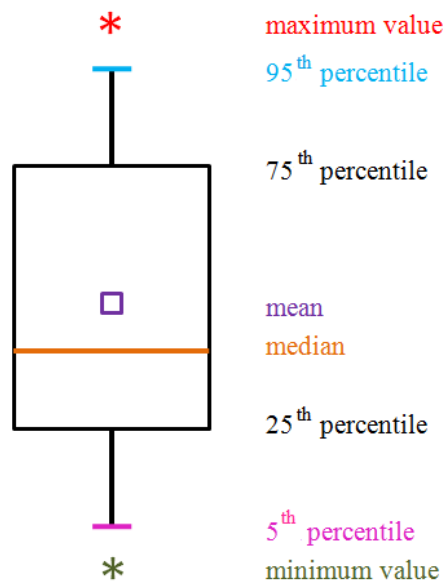


Figure 4.11: Corresponding values and ranges for box charts.

In addition, an example of distribution of data is presented in Figure 4.12 with different cases.

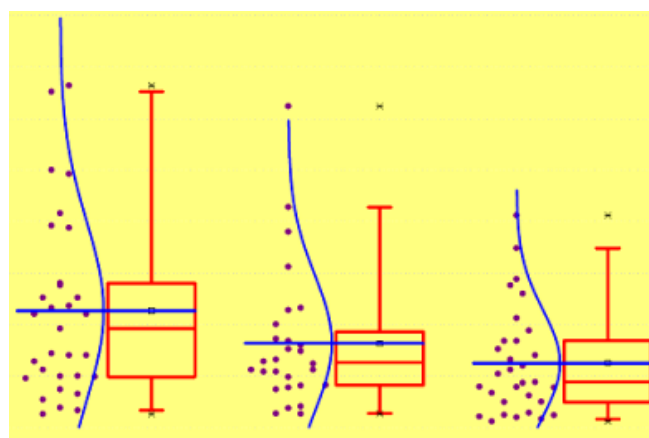


Figure 4.12: An example of data distribution for box charts [53].

In Figure 4.13, both the SERS measurements and EF values are represented in box charts for Ag NP spray coating and 10^{-4} M CV solution spin coating, spray coating of in-solution mixed Ag NPs + 10^{-4} M CV, Ag NP spray coating and 10^{-4} M BCB solution spin coating and spray coating of in-solution mixed Ag NPs + 10^{-4} M BCB in a, b, c, and d columns of the graph, respectively. In each column of the graph, corresponding statistics are represented for 20, 30 and 40 times pass numbers as indicated in table 4.1. For instance, 0.5, 0.9 and 1.1% surface coverage values correspond respectively to the 20, 30 and 40 times pass numbers of spray coating of colloidal Ag NP if it will be followed by spin coating of CV/BCB solutions, and that of spray coating of in-solution of Ag NP and CV/BCB solutions.

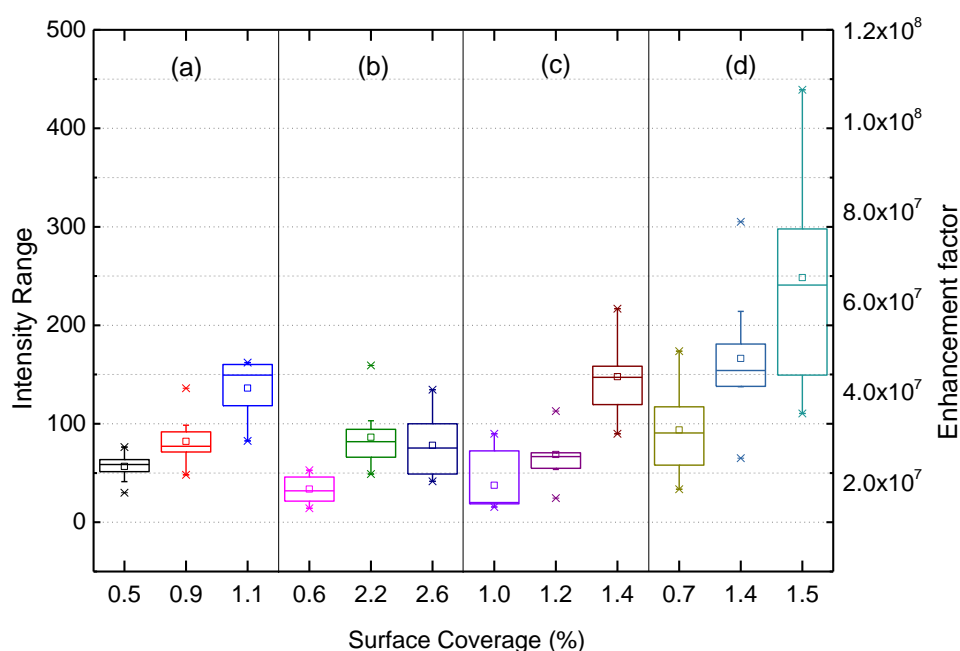


Figure 4.13: Box charts displaying the statistics of SERS measurements and enhancement factor for (a) Ag NP spray coating and 10^{-4} M CV solution spin coating, (b) spray coating of in-solution mixed Ag NPs + 10^{-4} M CV, (c) Ag NP spray coating and 10^{-4} M BCB solution spin coating, (d) spray coating of in-solution mixed Ag NPs + 10^{-4} M BCB.

Increase in the surface coverage values relates to the increase in the total number of Ag NPs and this allows hot spots to be formed at a higher probability. Hence, it can be deduced that when surface coverage increases, higher EF values are expected.

According to the Figure 4.13, the box charts that are represented in 4.13 could be considered as corresponding to this expectation. EF values range from 10^7 to 10^8 such that are close to the highest EF values that are obtained by surface averaged calculations in the literature.

SERS measurements and EF values of Ag NP spray coating and 10^{-5} M CV solution spin coating in Figure 4.14 (a), spray coating of in-solution mixed Ag NPs + 10^{-5} M CV in (b), Ag NP spray coating and 10^{-5} M BCB solution spin coating in (c), and spray coating of in-solution mixed Ag NPs + 10^{-5} M BCB are presented in (d).

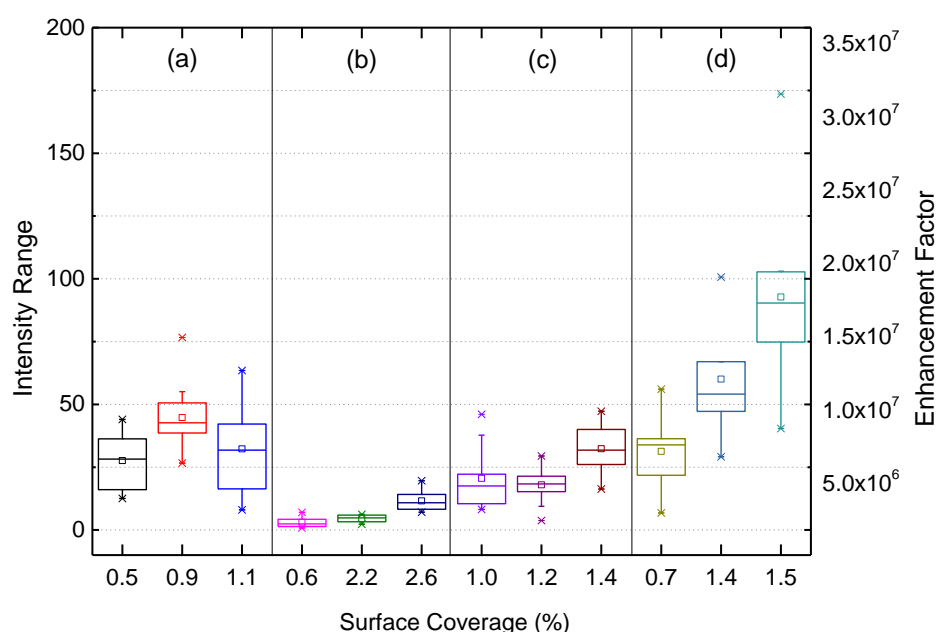


Figure 4.14: Box charts displaying the statistics of SERS measurements and enhancement factor for (a) Ag NP spray coating and 10^{-5} M CV solution spin coating, (b) spray coating of in-solution mixed Ag NPs + 10^{-5} M CV, (c) Ag NP spray coating and 10^{-5} M BCB solution spin coating, (d) spray coating of in-solution mixed Ag NPs + 10^{-5} M BCB.

When compared to the previous experimental results, generally same trend is observed; however, EF decreases because the total number of molecules adsorbed on metal nanostructures (N_{SERS}) decreases. Nevertheless, EF values are high enough to be between 10^6 and 10^7 .

In Figure 4.15, statistics of SERS measurements and EF are presented for substrates prepared by using 10^{-6} M CV and BCB. EF values vary between 10^5 and 10^6 . EF results of substrates prepared by Ag NP spray coating and 10^{-6} M CV solution spin coating (a) as compared to the other substrates ranges in a wider range. This corresponds to the low surface homogeneity of the samples.

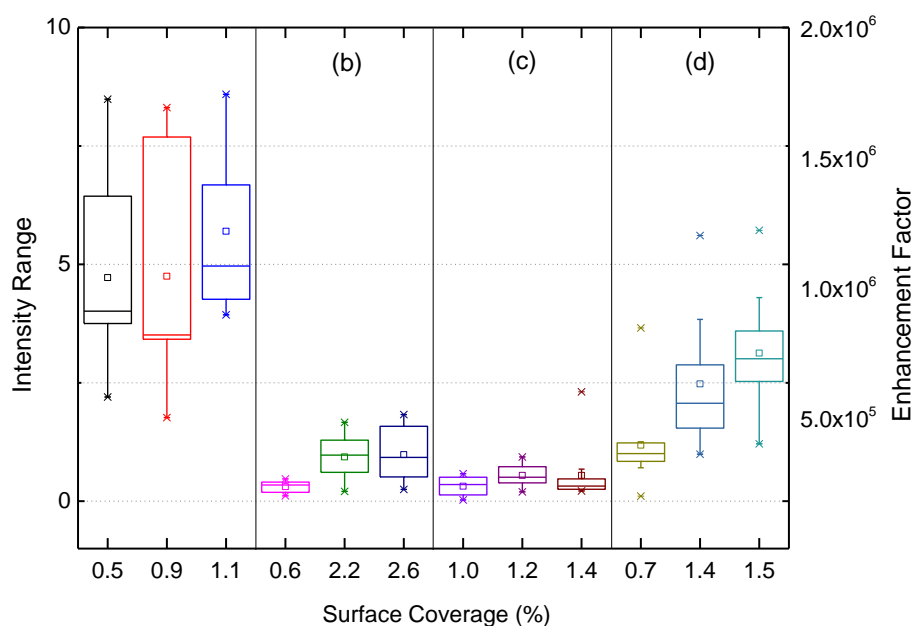


Figure 4.15: Box charts displaying the statistics of SERS measurements and enhancement factor for (a) Ag NP spray coating and 10^{-6} M CV solution spin coating, (b) spray coating of in-solution mixed Ag NPs + 10^{-6} M CV, (c) Ag NP spray coating and 10^{-6} M BCB solution spin coating, (d) spray coating of in-solution mixed Ag NPs + 10^{-6} M BCB.

In Figure 4.16, mean SERS intensity and linear fits of Ag NP spray coating and 10^{-4} , 10^{-5} , 10^{-6} M CV solution spin coating are presented. According to the mean SERS intensity values, SERS intensity increases when surface coverage increases as expected, except for result of substrate prepared by 10^{-5} M CV. In addition, increasing molarity of the molecules leads to the increasing mean SERS intensity.

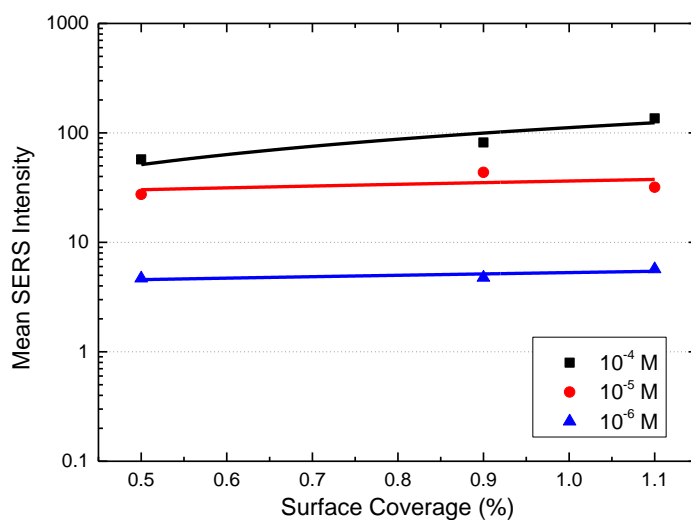


Figure 4.16: Mean SERS intensity obtained from box charts and linear fit of Ag NP spray coating and 10^{-4} , 10^{-5} , 10^{-6} M CV solution spin coating.

In Figure 4.17, mean SERS intensity and linear fits of spray coating of in-solution mixed Ag NPs + 10^{-4} , 10^{-5} , 10^{-6} M CV are presented.

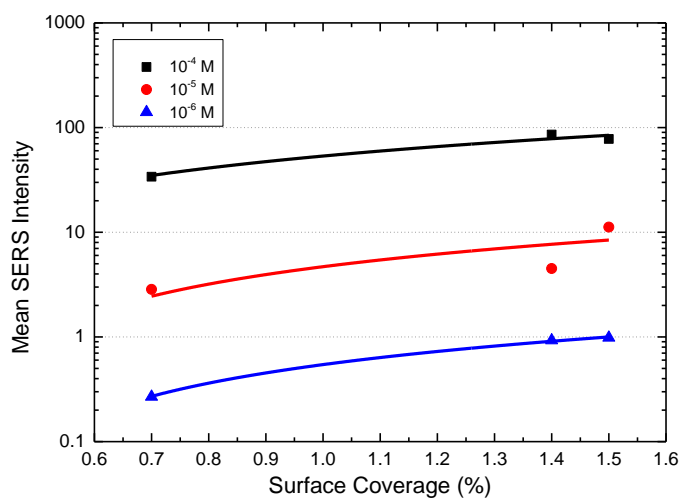


Figure 4.17: Mean SERS intensity obtained from box charts and linear fit of spray coating of in-solution mixed Ag NPs + 10^{-4} , 10^{-5} , 10^{-6} M CV.

It can be said that there is not a correlation between surface coverage and mean SERS intensity values, however increasing molecule molarities provides mean SERS intensity to increase.

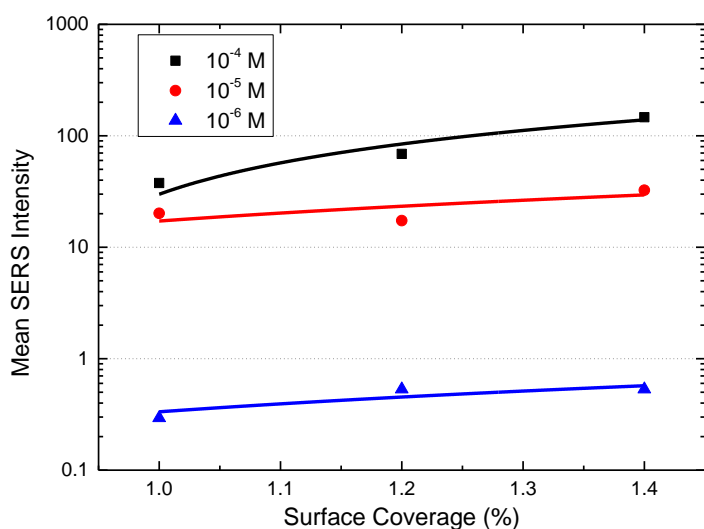


Figure 4.18: Mean SERS intensity obtained from box charts and linear fit of Ag NP spray coating and 10^{-4} , 10^{-5} , 10^{-6} M BCB solution spin coating.

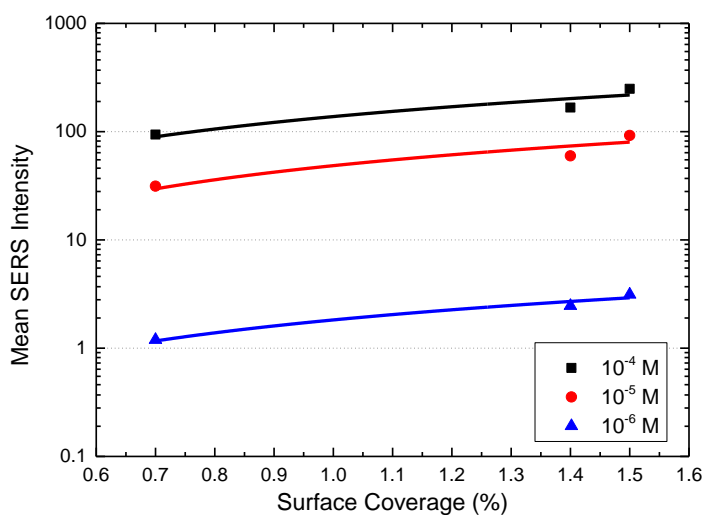


Figure 4.19: Mean SERS intensity obtained from box charts and linear fit of spray coating of in-solution mixed Ag NPs + 10^{-4} , 10^{-5} , 10^{-6} M BCB.

Figures 4.18 and 4.19 show mean SERS intensity and linear fit of Ag NP spray coating and 10^{-4} , 10^{-5} , 10^{-6} M BCB solution spin coating, and spray coating of in-solution mixed Ag NPs + 10^{-4} , 10^{-5} , 10^{-6} M BCB, respectively. Both increasing molarity and increasing surface coverage values provide mean SERS intensities to increase.

4.5. SEM Images and Reflection Results for Ag NWs

Surface coverage values for substrates that are prepared by colloidal Ag NWs and with 10^{-4} M CV and BCB were obtained by Gwyddion software as in the Ag NPs case. These values also used for 10^{-5} and 10^{-6} M CV and BCB containing substrates.

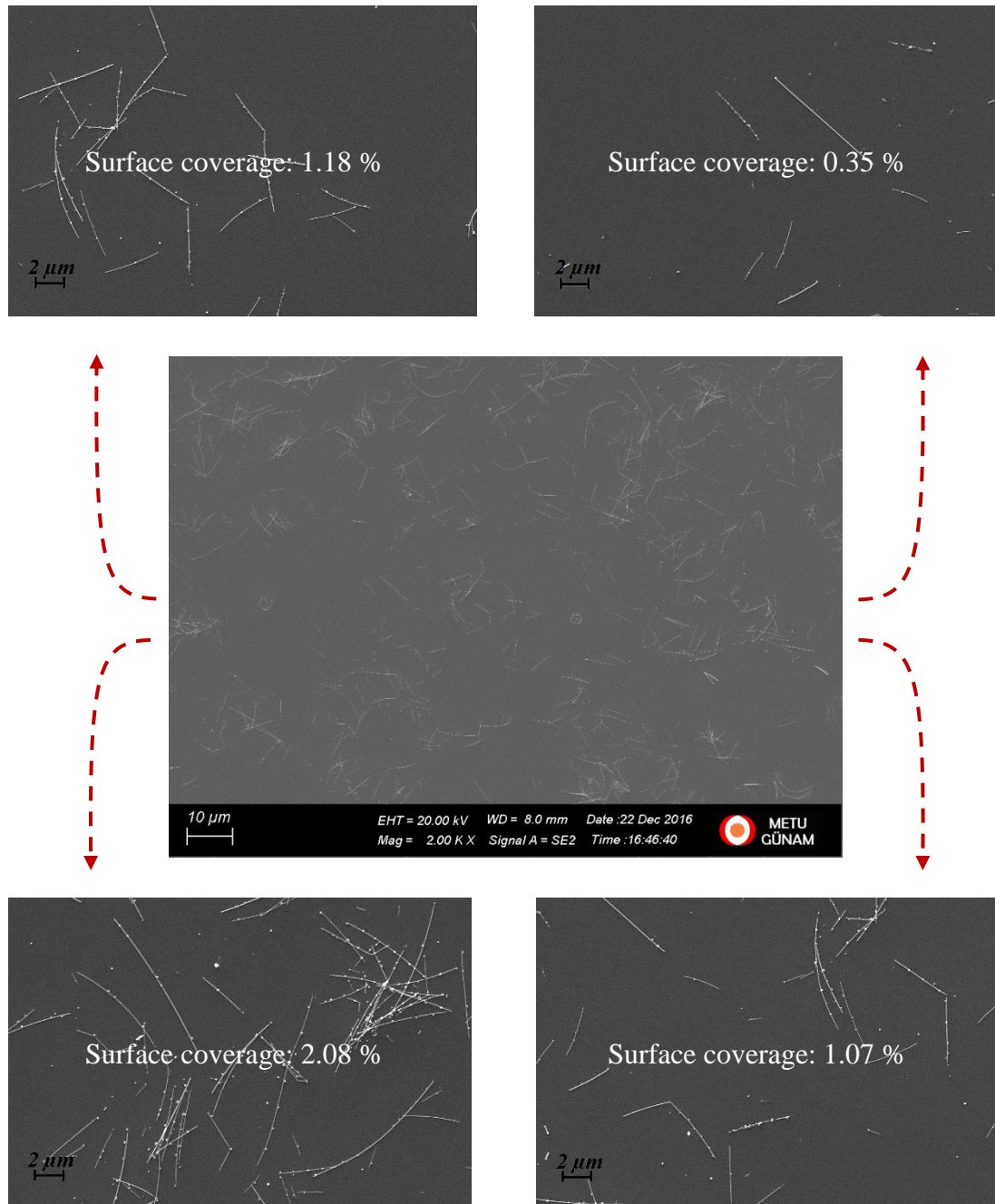


Figure 4.20: SEM image of 10^{-4} M CV spin coating on Ag NW spray coating with 20 times pass (middle) and images taken from 4 different locations of it.

However, number of grains and mean grain sizes could not be acquired due to the Ag NPs are contained in aqueous Ag NW suspensions as shown in Figure 4.20. Figure 4.21 SEM image of spray coating of in-solution mixed Ag NWs and BCB solution is represented. Surface coverage values are higher than that of previous method.

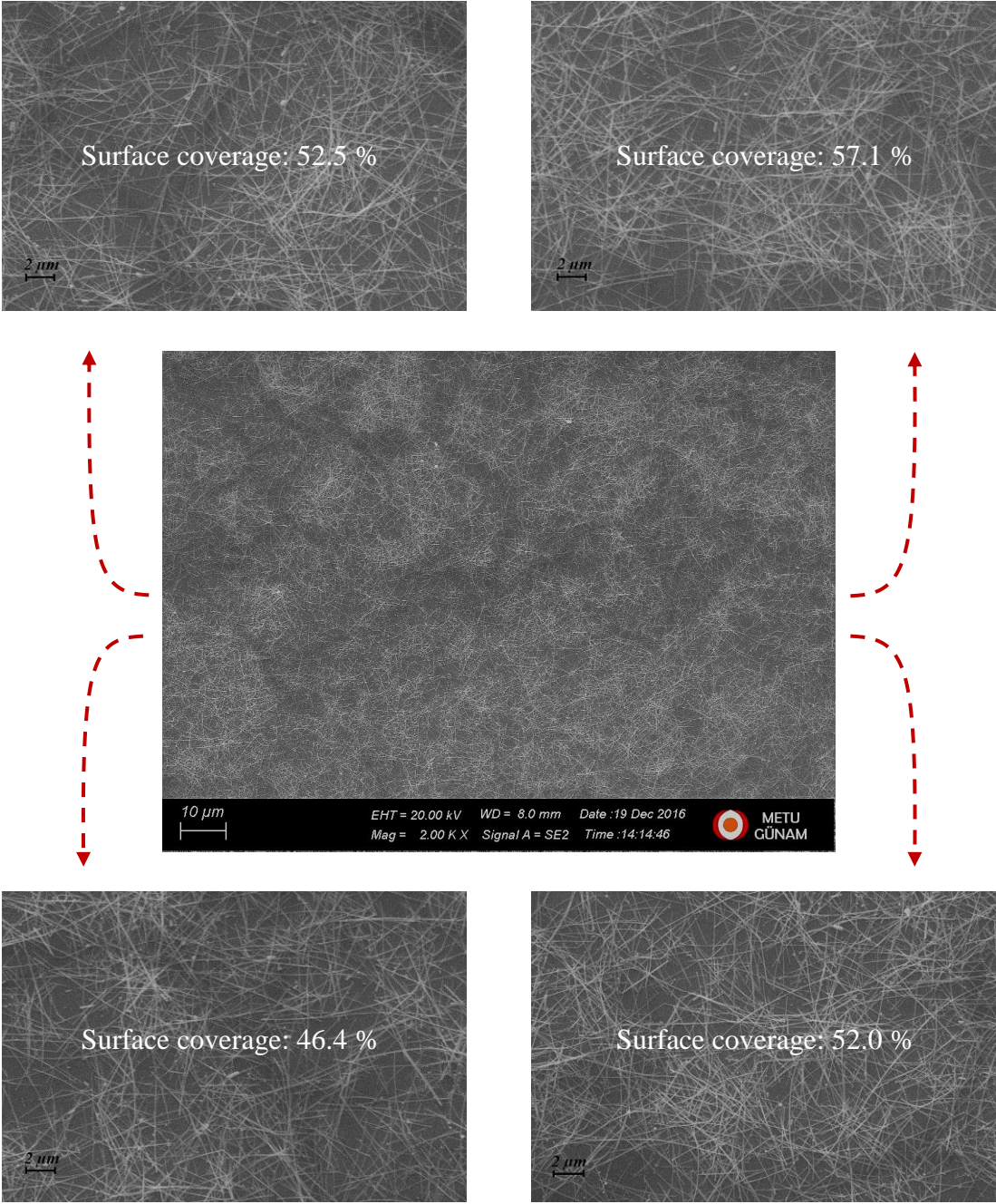


Figure 4.21: SEM image of spray coating of in-solution mixed Ag NWs with 20 times pass + $10^{-4}M$ BCB (middle) and images taken from 4 different locations of it.

Approximate lengths of the wires were detected by using distance measurement tool of Gwyddion program as shown in Figure 4.22.

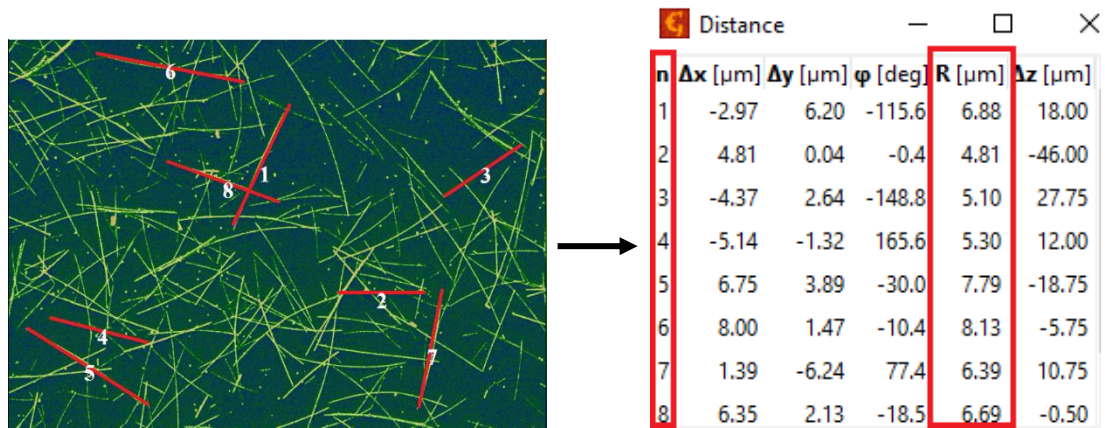


Figure 4.22: Approximated length of Ag NWs measured from SEM image of spray coating of colloidal Ag NWs with 30 times pass number and 10^{-4} M BCB spin coating.

Ag NW length range of selected 8 wires varies between 5-8 μm . Surface coverage values for corresponding substrate preparation methods are presented in table 4.2.

Table 4.2: Surface coverage values of Ag NWs for different substrate preparation techniques and 20, 30 and 40 times pass of Ag NWs.

	<i>Ag NW spray coating and CV spin coating</i>	<i>spray coating of in-solution mixed Ag NW and CV</i>	<i>Ag NW spray coating and BCB spin coating</i>	<i>spray coating of in-solution mixed Ag NW and BCB</i>
<i>20 times pass</i>	1.4	29.2	5.0	52.0
<i>30 times pass</i>	2.3	40.0	12.2	73.4
<i>40 times pass</i>	3.1	45.7	15.4	77.4

These results show that the substrates prepared by spray coating of in-solution mixed structures have a higher tendency to coat than substrates prepared by nanowire spray coating and molecule spin coating, which is why a large majority of some nanowires migrate from the surface when the molecule is spin coated.

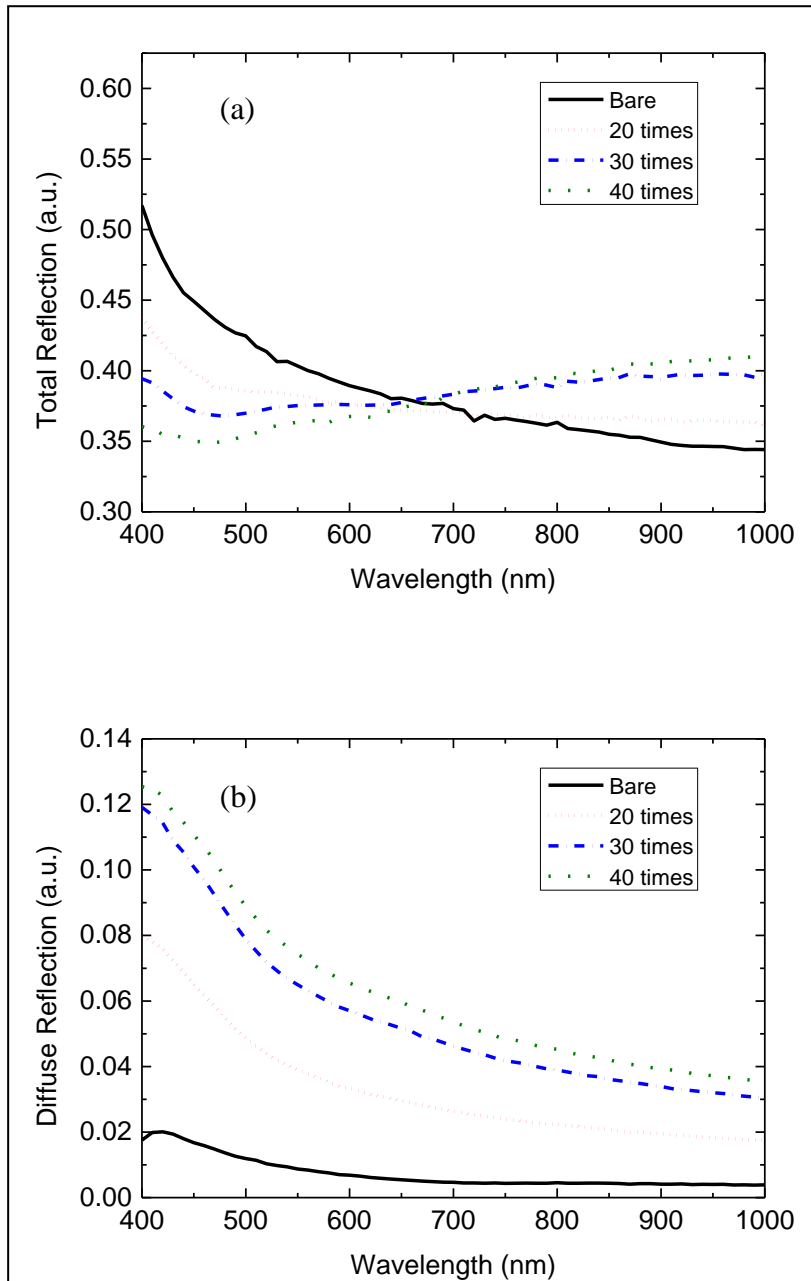


Figure 4.23: Total and diffuse reflection spectra of spray coating of in-solution mixed Ag NWs + 10^{-4} M CV for different number of passes.

Figure 4.23 (a) indicates that nanowires have different total reflection characteristics below and above 650 nm. As surface coverage of substrates increases, total reflection also increases at higher wavelengths than 650 nm; however, as surface coverage increases, total reflection decreases at the wavelengths below 650 nm. In Figure 4.23 (b) it is observed that when surface coverage increases, diffuse reflection also increases.

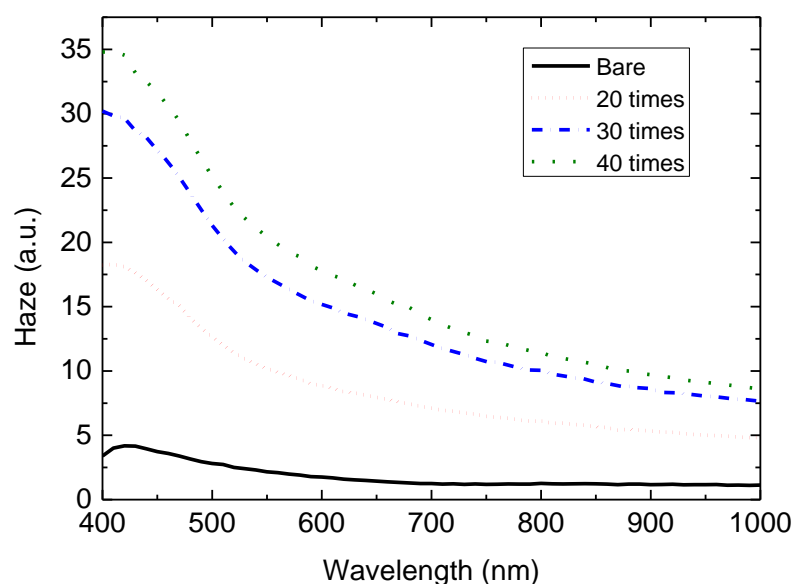


Figure 4.24: Haze spectrum of spray coating of in-solution mixed Ag NWs + 10^{-4} M CV for different number of passes.

Haze measurement results indicate that plasmon resonances for Ag NWs are observed at 400 nm as shown in Figure 4.24.

4.6. SERS Measurements for Ag NW and CV/BCB

Acquisition time was set as 250 seconds for samples that had been prepared by spray coating of colloidal Ag NW and spin coating of CV/BCB. Because of the saturation condition due to the high surface coverage of the samples, acquisition time for spray coating of in-solution mixed Ag NWs and CV/BCB on substrates was set as 10 seconds. SERS measurements were acquired from 10 different selected spots on prepared surfaces. Normalization for acquisition time and box chart representations were acquired same as the procedure for colloidal Ag NPs.

In Figure 4.25, SERS intensity spectra of Ag NW spray coating with 20 times pass and 10^{-4} M CV spin coating obtained from 10 different selected spots of substrate are presented. The selected peak and the area underneath are shown as in the case of Ag NP.

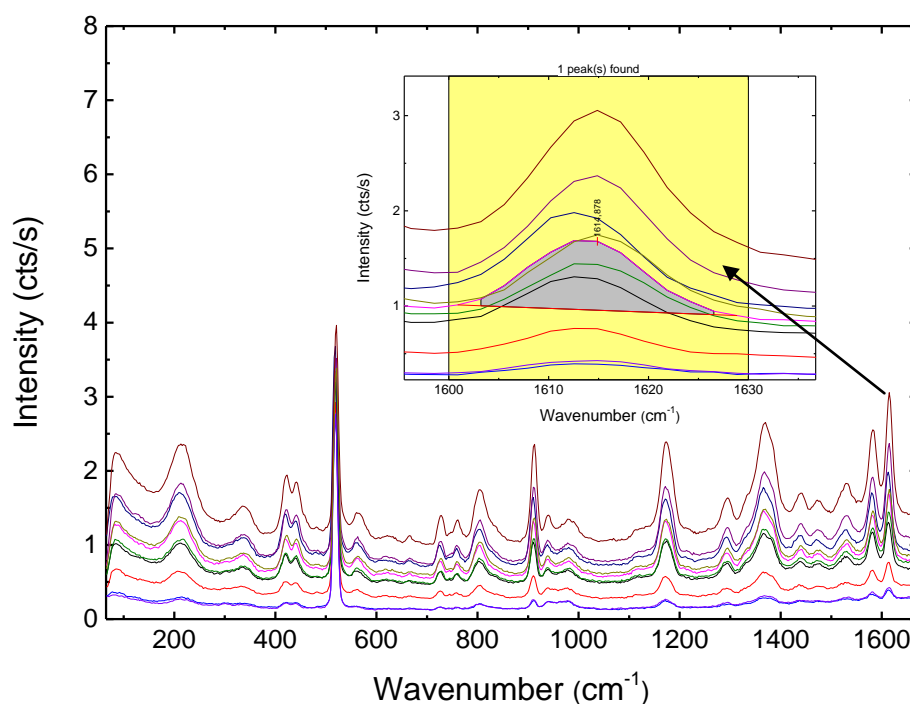


Figure 4.25: SERS intensity spectra of Ag NW spray coating with 20 times pass and 10^{-4} M CV spin coating obtained from 10 different selected spots of substrate and peak area under a strong peak between the 1600 and 1630 cm^{-1} to be used for statistics of SERS.

In Figure 4.26, Ag NW spray coating with 20 times pass number and 10^{-4} M BCB spin coating obtained from 10 different selected spots of substrate. One of the characteristic peaks of BCB was selected same as the Ag NP case and after baseline correction, area under these peaks were determined, and used to reveal the statistics of SERS measurements.

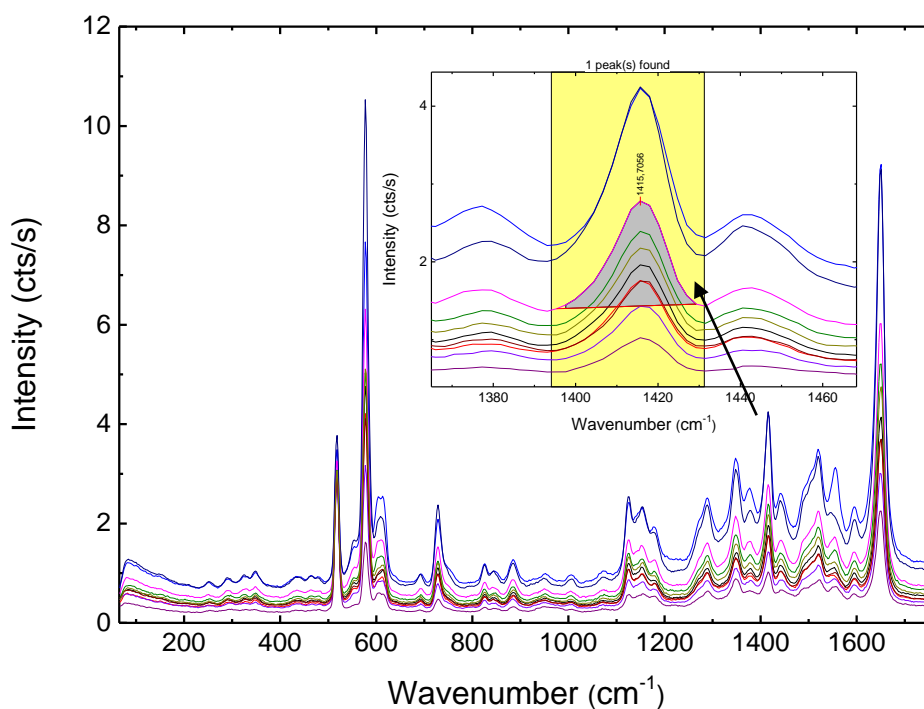


Figure 4.26: SERS intensity spectra of Ag NW spray coating with 20 times pass number and 10^{-4} M BCB spin coating obtained from 10 different selected spots of substrate and peak area under a strong peak between the 1395 and 1430 cm^{-1} to be used for statistics of SERS.

In Figure 4.27, statistics of SERS measurements for (a) Ag NW spray coating and 10^{-4} M CV solution spin coating and (b) Ag NW spray coating and 10^{-4} M BCB solution spin coating are shown with box charts. There is an increasing trend with increasing surface coverage for both methods. Although surface coverage of substrate having surface coverage of 12.2 % decreases compared to the 15.4 %, the increase in the EF can be attributed to the increase in the number of hot spots in the laser spot. In addition, this sample has a lower surface homogeneity as compared to the other substrates due to the higher difference between 75th and 25th percentage values in the corresponding box. Maximum EF acquired in case molecules locate in the Ag NP-Ag NW and Ag NW-Ag NW hot spots. Intensity range in column (a) indicates that the homogeneity of the substrates is high such that there is a proportional increase in the intensity range and there is not a huge difference between minimum and maximum values.

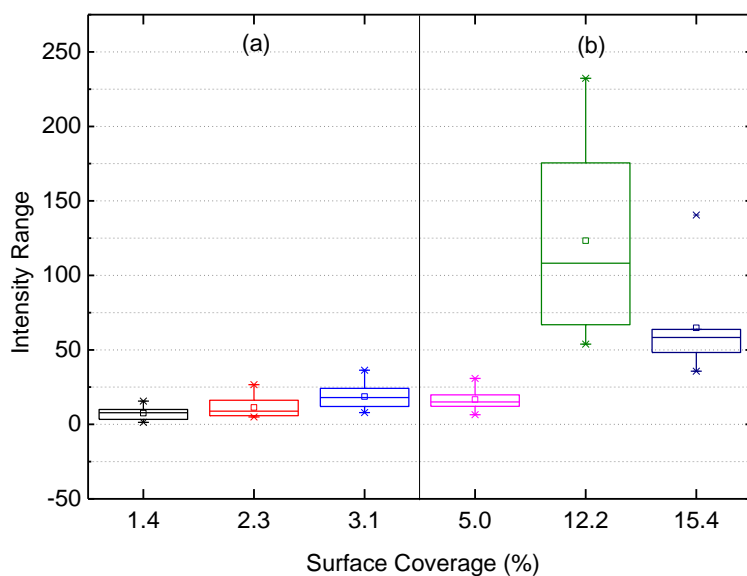


Figure 4.27: Box charts displaying the statistics of SERS measurements for (a) Ag NW spray coating and 10^{-4} M CV solution spin coating, (b) Ag NW spray coating and 10^{-4} M BCB solution spin coating.

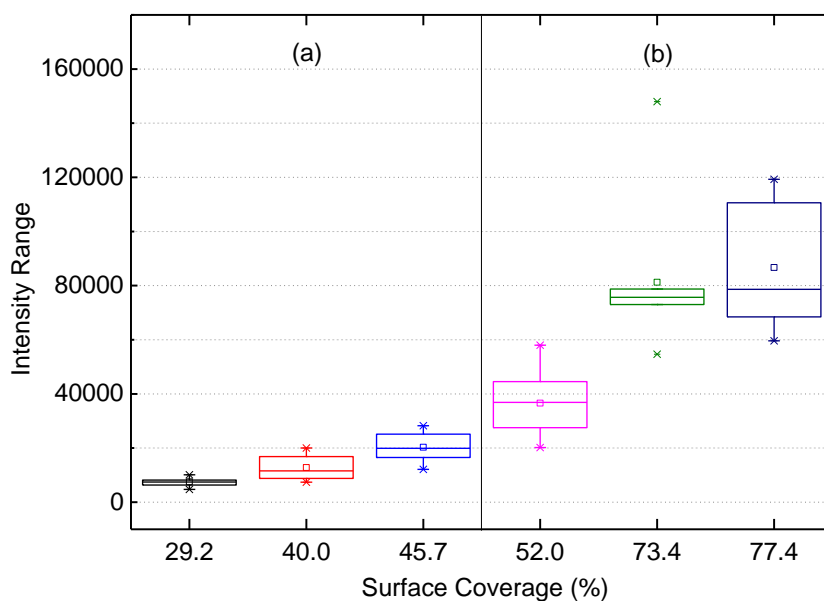


Figure 4.28: Box charts displaying the statistics of SERS measurements for (a) spray coating of in-solution mixed Ag NWs + 10^{-4} M CV, (b) spray coating of in-solution mixed Ag NWs + 10^{-4} M BCB.

In Figure 4.28, statistics of SERS measurements for (a) spray coating of in-solution mixed Ag NWs + 10^{-4} M CV, (b) spray coating of in-solution mixed Ag NWs + 10^{-4}

M BCB are shown. There is a huge increase in intensity range as compared to the previous method. Spray coating of in-solution mixed nanoparticles and molecules causes the surface to be highly coated. This allows a very high EF to be achieved because much more Ag NWs present in probe volume, and number of molecules located at hot spot of nanostructures increases.

In Figure 4.29, (a) Ag NW spray coating and 10^{-5} M CV solution spin coating and (b) Ag NW spray coating and 10^{-5} M BCB solution spin coating results are shown. Although the total number of adsorbed molecules on Ag nanostructures decreases, there is not a detectible trend in intensity range. However, intensity generally increases with increasing surface coverage in column (b) that can be seen from the mean values of the boxes.

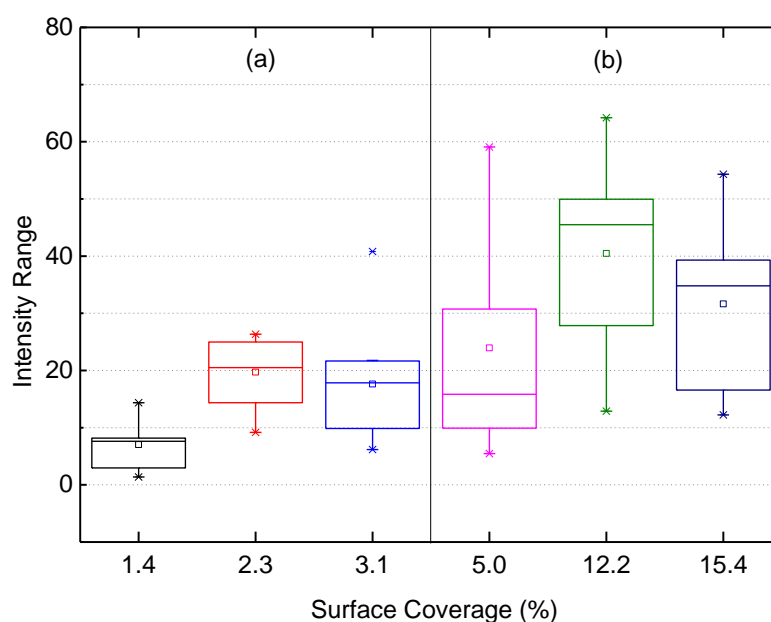


Figure 4.29: Box charts displaying the statistics of SERS measurements for (a) Ag NW spray coating and 10^{-5} M CV solution spin coating, (b) Ag NW spray coating and 10^{-5} M BCB solution spin coating.

Figure 4.30 shows the spray coating of in-solution mixed Ag NWs + 10^{-5} M CV in (a) and spray coating of in-solution mixed Ag NWs + 10^{-5} M BCB (b). Again intensity values tremendously increases as compared to the previous case that is prepared by spin coating of 10^{-5} M CV and BCB molecules due to high surface

coverage. However, when compared to the spray coating of in-solution mixed Ag NWs and 10^{-4} M CV/BCB, intensity range increases. This can be attributed to the smaller number of molecules adsorbed on metal nanostructures at a higher rate. The intensity range is increasing in accordance with the increase rate of the surface coverage in both columns (a) and (b).

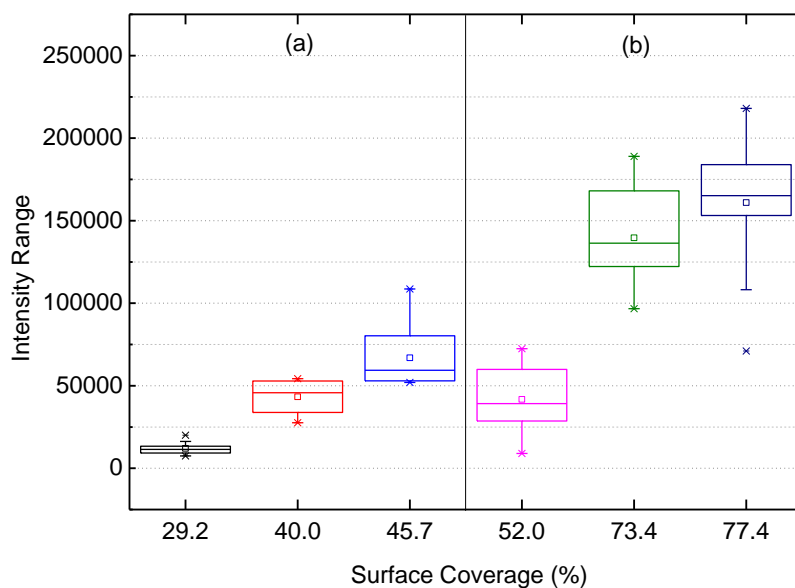


Figure 4.30: Box charts displaying the statistics of SERS measurements for (a) spray coating of in-solution mixed Ag NWs + 10^{-5} M CV, (b) spray coating of in-solution mixed Ag NWs + 10^{-5} M BCB.

Statistics of SERS measurements are presented for Ag NW spray coating and 10^{-6} M CV solution spin coating in Figure 4.31 (a), and Ag NW spray coating and 10^{-6} M BCB solution spin coating in (b). Although surface coverage of Ag NW spray coating and 10^{-6} M BCB solution spin coating is seems as 12.2 %, this value corresponds to the substrate that is prepared by same method but with 10^{-4} M BCB solution as indicated in SEM image results. It is obvious that surface coverage of Ag NW spray coating and 10^{-6} M BCB solution spin coating is more than 15.4 % due to the apparent increase in the mean value of intensity of this sample or molecules are adsorbed on metal nanostructures at a higher rate.

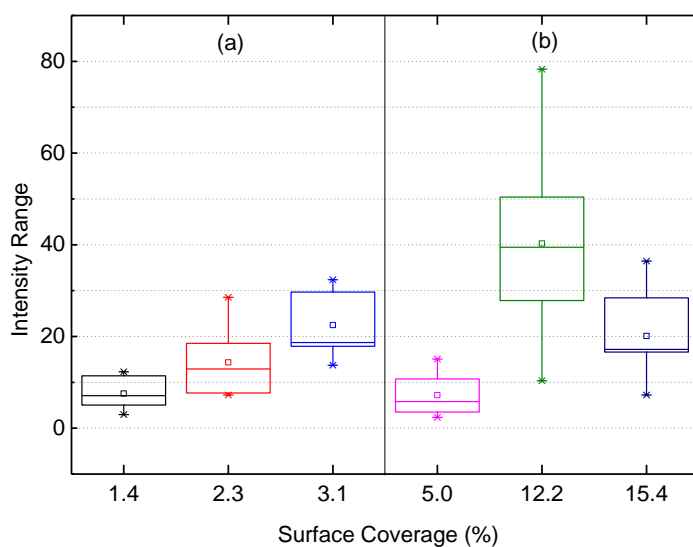


Figure 4.31: Box charts displaying the statistics of SERS measurements for (a) Ag NW spray coating and 10^{-6} M CV solution spin coating, (b) Ag NW spray coating and 10^{-6} M BCB solution spin coating.

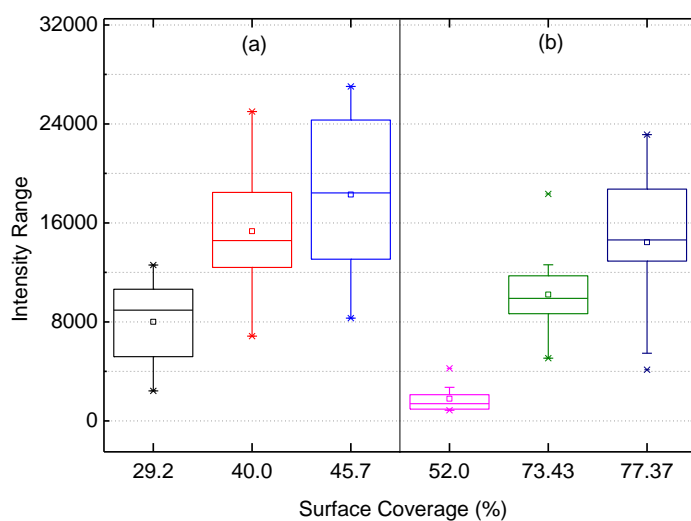


Figure 4.32 : Box charts displaying the statistics of SERS measurements for (a) spray coating of in-solution mixed Ag NWs + 10^{-6} M CV, (b) spray coating of in-solution mixed Ag NWs + 10^{-6} M BCB.

In Figure 4.32, statistics of SERS measurements of spray coating of in-solution mixed Ag NWs + 10^{-6} M CV and spray coating of in-solution mixed Ag NWs + 10^{-6}

M BCB are shown in (a) and (b), respectively. It can be concluded that intensity range is much higher than that of the previous results and much lower than that of the substrates that are prepared by the same method but with molecules of 10^{-5} M as expected.

In Figures 4.33, 4.34, 4.35 and 4.36, mean SERS intensity obtained from box charts and linear fit of all the methods that are prepared by Ag NWs are presented. Generally, there is not a trend related to molarities of molecules and mean SERS intensity relation.

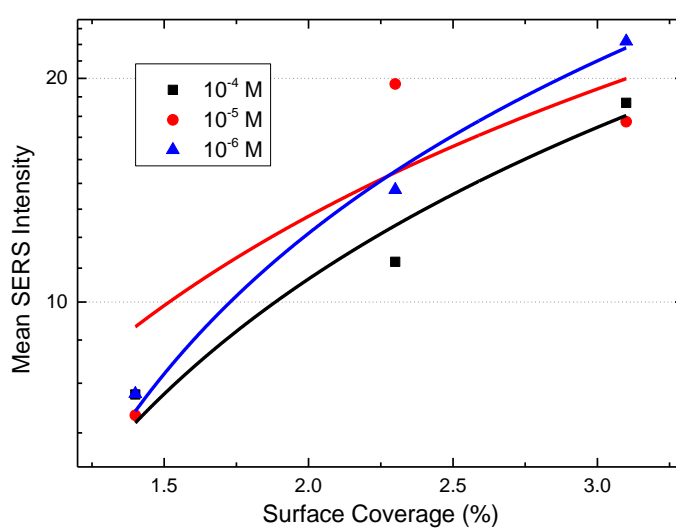


Figure 4.33: Mean SERS intensity obtained from box charts and linear fit of Ag NW spray coating and 10^{-4} , 10^{-5} , 10^{-6} M CV solution spin coating.

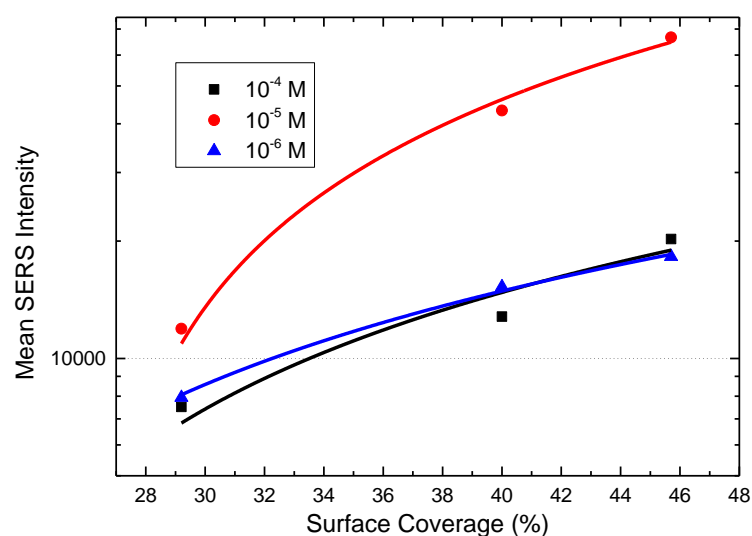


Figure 4.34: Mean SERS intensity obtained from box charts and linear fit of spray coating of in-solution mixed Ag NWs + 10^{-4} , 10^{-5} , 10^{-6} M CV.

Only linear fit of Ag NW spray coating and 10^{-4} , 10^{-5} , 10^{-6} M BCB solution spin coating substrates reveals that increasing molarity provides SERS intensity range to increase as shown in Figure 4.35.

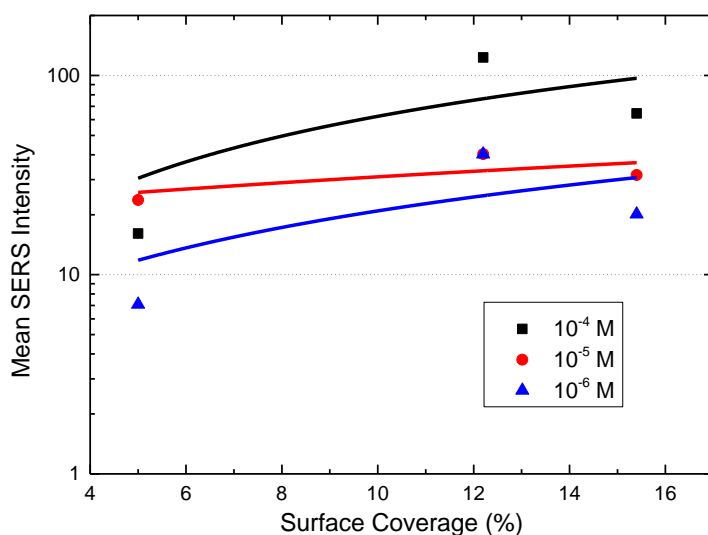


Figure 4.35: Mean SERS intensity obtained from box charts and linear fit of Ag NW spray coating and 10^{-4} , 10^{-5} , 10^{-6} M BCB solution spin coating.

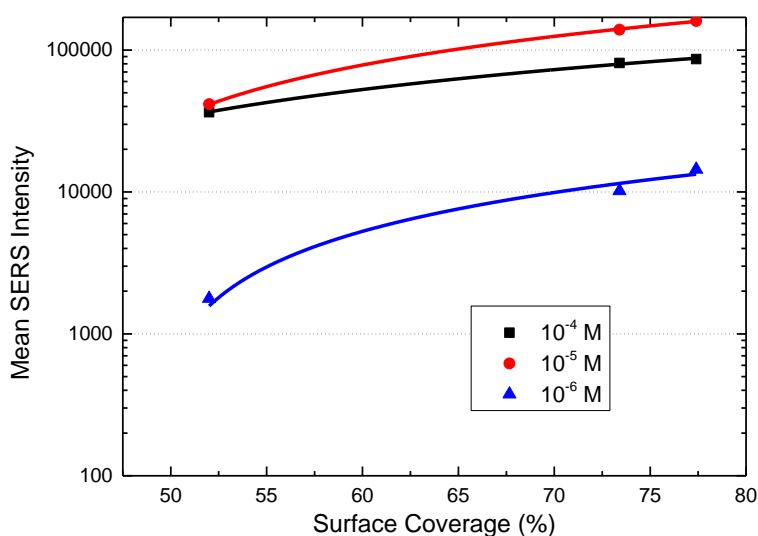


Figure 4.36: Mean SERS intensity obtained from box charts and linear fit of spray coating of in-solution mixed Ag NWs + 10^{-4} , 10^{-5} , 10^{-6} M BCB.

In addition, it could be said that increasing surface coverage provides mean SERS intensity obtained from box charts to increase in general.

4.7. Simulation

To compare the experimental and theoretical EF values, some simulations were conducted by MNP-BEM simulation program. Maxwell's equations were solved in 3D with boundary element method. By this method, surface charge densities are calculated and these values are converted to the field amplitudes over the surface by using Green's function. Simulations were prepared by placing dimer nanoparticles radius of 50 nm located on a 400 x 400 mesh grid. The distances between these dimers were set as 2, 5, 10 and 20 nm. Then, x-polarized and 532 nm incident light was used to investigate the electric field distribution, and compare how the EF changes with distance between dimers. In Figure 4.37, electric field distribution between and around the nanoparticles are presented according to the simulation results. When the distance between nanoparticles decreases, field amplitudes increase. In the case of hot spot between the nanoparticles, EF strongly increases. In Figure 4.37 (c) and (d) distances between the nanoparticles are 5 and 2 nm that correspond to the distances that allow hot spots to be achieved.

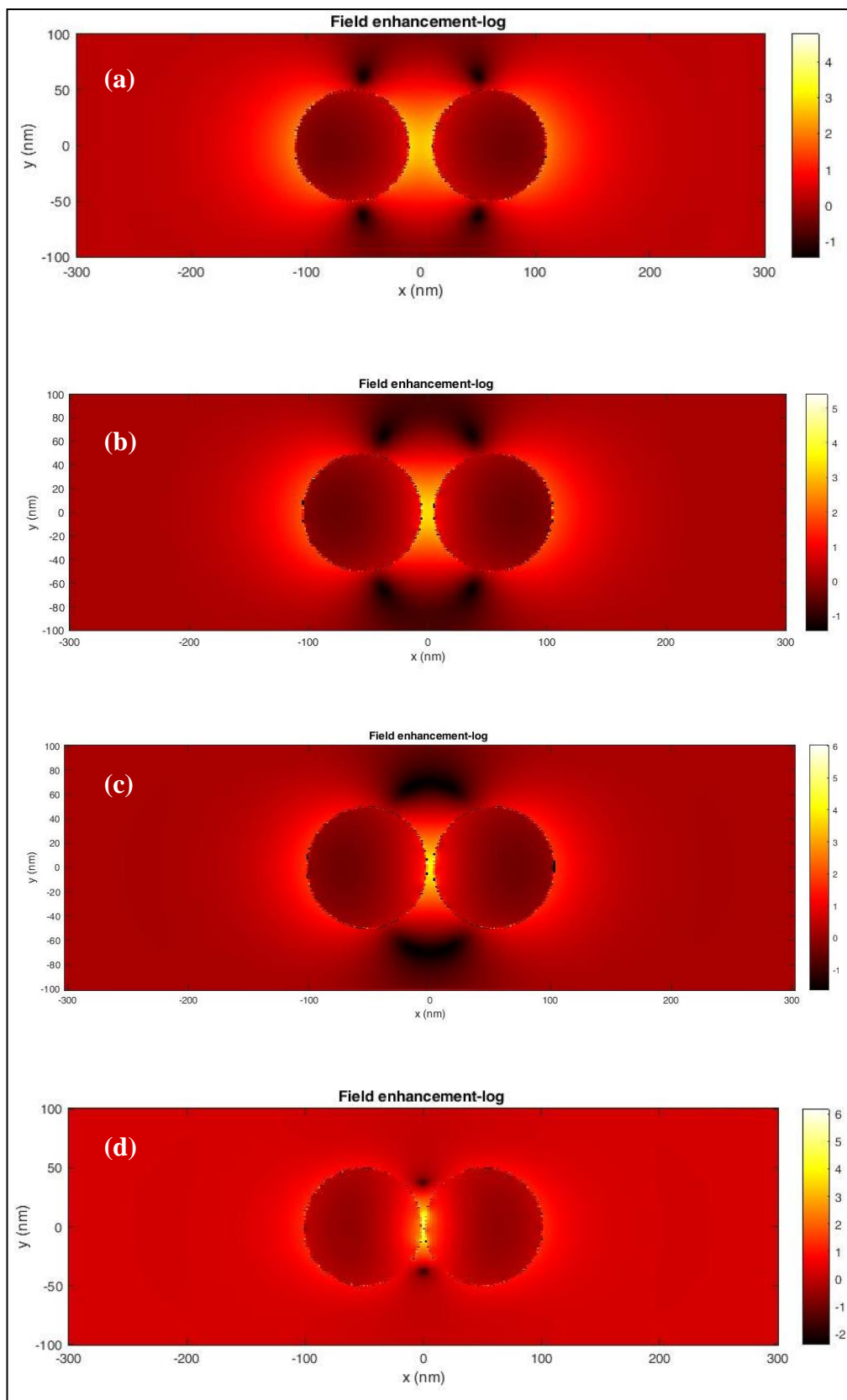


Figure 4.37: Electric field distribution of a 100 nm dimer obtained by locating (a) 20, (b) 10, (c) 5, (d) 2 nm away from each other.

Theoretical EF was calculated by $EF_{\text{SERS}} = |E(r)|^4/|E_0(r)|^4$ as indicated in section 2.4, EF is proportional to the fourth power of the electric field amplitude at a point with respect to that of incident electric field.

Amplitude of $E_0(r)$ was determined as 1.3 by locating dimer far away from each other with ensuring that this value does not change after that point. EF was calculated using the maximum electric field amplitude taken from the surface above 50 nm.

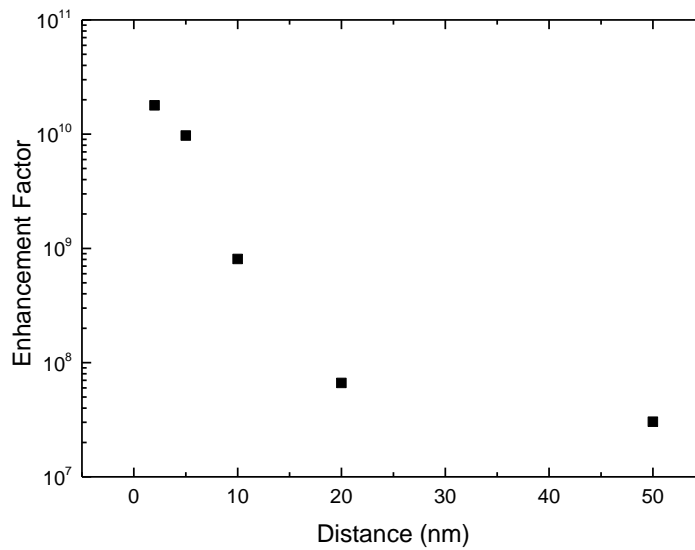


Figure 4.38: Enhancement factor graph for dimers (radius of 50 nm) located on a 400 x 400 mesh grid at a distance of 2, 5, 10, 20 and 50 nm from each other.

EF tremendously increases when the gap size between the nanoparticles is 2 nm and reduces when the inter-particle distance increases as shown in Figure 4.38.

CHAPTER 5

CONCLUSIONS

In this thesis study, SERS activity of polyol synthesized colloidal Ag NPs and Ag NWs were investigated by interacting these nanostructures with CV and BCB analytes. Experimental procedure consists of two type of substrate preparation. One method is decorating Si wafers with colloidal Ag NP/Ag NW by spray coating, and then spin coating of CV/BCB molecules on them. Other method is spray coating of in-solution mixed colloidal Ag NP/Ag NW and CV/BCB solutions. Spray coating was carried out as 20, 30 and 40 times passing for each substrate. These different numbers of passes were characterized by SEM image analysis revealing generally increasing surface coverage values with increasing passing numbers. Although the expected surface homogeneity could not be obtained, generally the effect of increasing number of nanostructures that are obtained from SEM images could be analyzed from the statistics of EF values that are presented by box charts for substrates that are prepared by colloidal Ag NPs. Due to the fact that mean grain size and number of grains could not be analyzed properly, corresponding EF values for colloidal Ag NWs could not be calculated.

As indicated in section 2.3.1.3, Ag NP has strong extinction and Ag NW has two peaks corresponding to transverse oscillations corresponding LSPR bands. Extinction spectrum for metal nanostructures gives idea about enhancement effect. When Ag NPs and Ag NWs interact with CV and BCB molecules, these bands red shift owing to dipole–dipole interactions and surface plasmon coupling between aggregated nanostructures. In addition, absorption maximum wavelengths of CV and BCB solutions correspond to 590 and 622 nm, respectively. Absorption peaks of aqueous solutions of CV/BCB molecules and extinction peaks of colloidal Ag NP/Ag NW are not resonance with Raman laser light. Laser light wavelength is

between the LSP bands and absorption peak maximums of CV and BCB. Hence, highly strong EF values are obtained in this study. In addition, wavelength of laser light is close to the absorption peak of CV, so more EF values are expected from substrates that are prepared by using CV. However, this trend generally can not be observed within the scope of this study.

Longer plasmon lifetimes can be obtained via smooth crystalline surfaces of polyol synthesized Ag NPs and Ag NWs when coupling of these nanostructures are considered. In the scope of this study, it can be concluded that increase in the lifetime of plasmons provide nanostructures to interact strongly.

By the help of box charts we have gained statistics of SERS measurements and we could compare them with the corresponding surface coverage of the samples. In addition, we have analyzed the surface homogeneity and hot spot generation through spray coating of Ag NP and Ag NW on Si wafers. We used Si Raman peak at 521 cm^{-1} to calibrate the spectra that we obtained from Raman and SERS measurements. One of the strongest Raman peaks of CV (1614 cm^{-1}) and BCB (1419 cm^{-1}) were used to reveal statistics of SERS measurements by baseline correction and calculation of area under corresponding bands of these sharp peaks. Mean SERS intensity increases with increasing Ag NP surface coverage and molarity of CV and BCB as expected. The data that deviate from this trend is caused as a result of poor surface homogeneity. However, this kind of trend for molarity could not been achieved from the linear fits of mean SERS intensity values for Ag NWs.

Literature review indicates that average SERS EF could be between 10 and 10^3 for poor experimental conditions. Range of 10^5 - 10^6 could be achieved often. EF between 10^7 and 10^8 can be obtained through very well prepared substrates and in the suitable experimental conditions. In this study we have achieved as high as maximum values indicated at SERS literature. Furthermore, EFs for substrates prepared by Ag NWs are more promising than Ag NPs when intensity range of them is compared to the Ag NPs.

Simulation results suggest that when the nanoparticles are positioned at a distance of at most a few nanometers from each other, EF has indicated to be tremendously high. Hence, maximum EF is obtained from molecules that are located at the hot spots.

According to the simulation results, maximum achievable EF is as high as 1.8×10^{10} . This value obtained by considering the maximum electric field amplitude at the hot spot of two perfect spherical nanoparticles. However, experimental setup measures the signal from randomly adsorbed molecules on metal nanostructures and averages over the probe volume. So, EF about 10^8 that we achieved from the calculations is not as high as the simulation results.

REFERENCES

- [1] K. Kneipp, H. Kneipp, I. Itzkan, R. P. Dasari, and M. S. Feld, "Surface-enhanced Raman scattering and biophysics," *J. Phys. Condens. Matter*, vol. 14, no. 18, pp. R597–R624, 2002.
- [2] K. Wilson and J. Walker, *Principles and Techniques of Biochemistry and Molecular Biology*, 7th ed. Cambridge University Press, 2010.
- [3] M. A. Garcia, "Surface plasmons in metallic nanoparticles: fundamentals and applications," *J. Phys. D. Appl. Phys.*, vol. 44, no. 28, pp. 1–20, 2011.
- [4] H. H. Nguyen, J. Park, S. Kang, and M. Kim, "Surface plasmon resonance: A versatile technique for biosensor applications," *Sensors (Switzerland)*, vol. 15, no. 5, pp. 10481–10510, 2015.
- [5] F. Rouessac and A. Rouessac, *Chemical Analysis: Modern Instrumentation Methods and Techniques*, 2nd ed. Wiley, 2007.
- [6] D. L. Jeanmaire and R. P. Van Duyne, "Surface raman spectroelectrochemistry," *Journal of Electroanalytical Chemistry and Interfacial Electrochemistry*, vol. 84, no. 1, pp. 1–20, 1977.
- [7] M. G. Albrecht and J. A. Creighton, "Anomalously intense Raman spectra of pyridine at a silver electrode," *J. Am. Chem. Soc.*, vol. 99, no. 15, pp. 5215–5217, 1977.
- [8] S. Fateixa, H. I. S. Nogueira, and T. Trindade, "Hybrid nanostructures for SERS: materials development and chemical detection," *Phys. Chem. Chem. Phys.*, vol. 17, no. 33, pp. 21046–21071, 2015.
- [9] E. C. Le Ru and P. Etchegoin, *Principles of Surface Enhanced Raman Spectroscopy*, 1st ed. Amsterdam: Elsevier, 2009.
- [10] C. V. Raman and K. S. Krishnan, "A new type of secondary radiation," *Nature*, vol. 121, no. 3048, pp. 501–502, 1928.
- [11] M. Fleischmann, P. J. Hendra, and A. J. McQuillan, "Raman spectra of pyridine at a silver electrode," *Chem. Phys. Lett.*, vol. 26, no. 2, pp. 163–166, 1974.
- [12] R. P. Van Duyne, "Surface-enhanced Raman sensors: early history and the development of sensors for quantitative biowarfare agent and glucose detection," *J. Raman Spectrosc.*, vol. 36, no. 6–7, pp. 471–484, 2005.
- [13] K. Kneipp, Y. Wang, H. Kneipp, L. T. Perelman, and I. Itzkan, "Single molecule detection using surface-enhanced Raman scattering (SERS)," *Phys. Rev. Lett.*, vol. 78, no. 9, pp. 1667–1670, 1997.
- [14] H. Xux and M. Käll, "Polarization-dependent surface-enhanced Raman spectroscopy of isolated silver nanoaggregates," *ChemPhysChem*, vol. 4, no. 9, pp. 1001–1005, 2003.
- [15] A. Bek, R. Jansen, M. Ringler, S. Mayilo, T. A. Klar, and J. Feldmann, "Fluorescence enhancement in hot spots of AFM-designed gold nanoparticle sandwiches," *Nano Lett.*, vol. 8, no. 2, pp. 485–490, 2008.
- [16] K. Kneipp, "Surface-enhanced Raman scattering," *Phys. Today*, vol. 60, no. 11, pp. 40–46, 2007.
- [17] P. L. Stiles, J. A. Dieringer, N. C. Shah, and R. P. Van Duyne, "Surface-

- enhanced Raman spectroscopy,” *Annu. Rev. Anal. Chem.*, vol. 1, no. 1, pp. 601–626, 2008.
- [18] P. Vandenabeele, *Practical Raman Spectroscopy*. Wiley, 2013.
- [19] P. Gillet, “La cellule à enclumes de diamant,” 2004. [Online]. Available: <http://planet-terre.ens-lyon.fr/article/cellule-diamant.xml>. [Accessed: 02-Jan-2017].
- [20] S. A. Maier, *Plasmonics: Fundamentals and Applications*. New York: Springer, 2007.
- [21] L. Novotny and B. Hecht, *Principles of Nano-Optics*, 1st ed. New York: Cambridge, 2006.
- [22] A. Z. D. Richards, *Nano-Optics and Near-Field Optical Microscopy*, 1st ed. London: Artech House, 2009.
- [23] M. L. Weber and K. a. Willets, “Nanoscale studies of plasmonic hot spots using super-resolution optical imaging,” *MRS Bull.*, vol. 37, no. 8, pp. 745–751, 2012.
- [24] F. L. Pedrotti, L. S. Pedrotti, and L. M. Pedrotti, *Introduction to Optics*, 3rd ed. 2007.
- [25] B. E. A. Saleh and M. C. Teich, *Fundamentals of Photonics*, 1st ed. New York: Wiley, 1991.
- [26] J. Li and N. Wu, “Biosensors Based on Nanomaterials and Nanodevices,” CRC Press, 2013.
- [27] K. L. Wustholz *et al.*, “Structure-activity relationships in gold nanoparticle dimers and trimers for surface-enhanced Raman spectroscopy,” *J. Am. Chem. Soc.*, vol. 132, no. 31, pp. 10903–10910, 2010.
- [28] R. Aroca, *Surface Enhanced Vibrational Spectroscopy*. Hoboken, NJ: Wiley, 2006.
- [29] P. G. Etchegoin and E. C. Le Ru, “Basic electromagnetic theory of SERS,” in *Surface Enhanced Raman Spectroscopy: Analytical, Biophysical and Life Science Applications*, S. Schlücker, Ed. Weinheim: Wiley-VCH, 2011, pp. 1–37.
- [30] R. J. Newhouse and J. Z. Zhang, “Optical properties and applications of shape-controlled metal nanostructures,” in *Reviews in Plasmonics*, C. D. Geddes, Ed. Springer, 2012, pp. 205–238.
- [31] I. Long, G. Mie, and R. Ritchie, *Plasmonics*. 1957.
- [32] E. Hutter and J. H. Fendler, “Exploitation of localized surface plasmon resonance,” *Adv. Mater.*, vol. 16, no. 19, pp. 1685–1706, 2004.
- [33] K. A. Willets and R. P. Van Duyne, “Localized surface plasmon resonance spectroscopy and sensing,” *Annu. Rev. Phys. Chem.*, vol. 58, pp. 267–297, 2007.
- [34] K. L. Kelly, E. Coronado, L. L. Zhao, and G. C. Schatz, “The optical properties of metal nanoparticles: the influence of size, shape, and dielectric environment,” *J. Phys. Chem. B*, vol. 107, no. 3, pp. 668–677, 2003.
- [35] X. Huang, “Gold Nanoparticles Used in Cancer Cell Diagnostics, Selective Photothermal Therapy and Catalysis of NADH Oxidation Reaction,” 2006.
- [36] Q. N. Luu, J. M. Doorn, M. T. Berry, C. Jiang, C. Lin, and P. S. May, “Preparation and optical properties of silver nanowires and silver-nanowire thin films,” *J. Colloid Interface Sci.*, vol. 356, no. 1, pp. 151–158, 2011.
- [37] S. Kim, K. Imura, M. Lee, T. Narushima, H. Okamoto, and D. H. Jeong, “Strong optical coupling between mutually orthogonal plasmon oscillations in

- a silver nanosphere-nanowire joined system.,” *Phys. Chem. Chem. Phys.*, vol. 15, no. 12, pp. 4146–53, 2013.
- [38] R. Sanci and M. Volkan, “Surface-enhanced Raman scattering (SERS) studies on silver nanorod substrates,” *Sensors Actuators, B Chem.*, vol. 139, no. 1, pp. 150–155, 2009.
- [39] G. C. Schatz, M. A. Young, and R. P. Duyne, “Electromagnetic mechanism of SERS,” in *Surface-Enhanced Raman Scattering*, 1st ed., vol. 103, K. Kneipp, M. Moskovits, and H. Kneipp, Eds. Berlin: Springer, 2006, pp. 19–45.
- [40] C. Haynes and R. Van Duyne, “Plasmon-sampled surface-enhanced Raman excitation spectroscopy,” *J. Phys. Chem. B*, vol. 107, pp. 7426–7433, 2003.
- [41] S. Gwo, H.-Y. Chen, M.-H. Lin, L. Sun, and X. Li, “Nanomanipulation and controlled self-assembly of metal nanoparticles and nanocrystals for plasmonics,” *Chem. Soc. Rev.*, vol. 45, no. 20, pp. 5672–5716, 2016.
- [42] B. C. Yildiz *et al.*, “Enhanced second harmonic generation from coupled asymmetric plasmonic metal nanostructures,” *J. Opt.*, vol. 17, no. 12, p. 125005, 2015.
- [43] E. C. Le Ru, M. Meyer, P. G. Etchegoin, and E. Blackie, “Surface enhanced Raman scattering enhancement factors: a comprehensive study,” *J. Phys. Chem. C*, vol. 111, no. 37, pp. 13794–13803, 2007.
- [44] M. D. Sonntag, J. M. Klingsporn, A. B. Zrimsek, B. Sharma, L. K. Ruvuna, and R. P. Van Duyne, “Molecular plasmonics for nanoscale spectroscopy,” *Chem. Soc. Rev.*, vol. 43, no. 4, pp. 1230–47, 2014.
- [45] R. W. Sabnis, *Handbook of Biological Dyes and Stains*. New Jersey: John Wiley & Sons, Inc., 2010.
- [46] S. Coskun, B. Aksoy, and H. E. Unalan, “Polyol synthesis of silver nanowires: An extensive parametric study,” *Cryst. Growth Des.*, vol. 11, no. 11, pp. 4963–4969, 2011.
- [47] S. Xie, Z. Ouyang, B. Jia, and M. Gu, “Large-size, high-uniformity, random silver nanowire networks as transparent electrodes for crystalline silicon wafer solar cells,” *Opt. Express*, vol. 21, no. S3, pp. A355–A362, 2013.
- [48] A. E903-12, “Standard Test Method for Solar Absorptance, Reflectance, and Transmittance of Materials Using Integrating Spheres,” 2013.
- [49] J. Beaulieu, “A guide to integrating sphere theory and applications,” 1999.
- [50] I. Tanyeli, H. Nasser, F. Es, A. Bek, and R. Turan, “Effect of surface type on structural and optical properties of Ag nanoparticles formed by dewetting,” *Opt. Express*, vol. 21, no. 18, pp. A798–A807, 2013.
- [51] K. Lai, Y. Zhang, R. Du, F. Zhai, B. A. Rasco, and Y. Huang, “Determination of chloramphenicol and crystal violet with surface enhanced Raman spectroscopy,” *Sens. Instrum. Food Qual. Saf.*, vol. 5, no. 1, pp. 19–24, 2011.
- [52] S. Saatci, B. C. Yildiz, A. Bek, and M. E. Tasgin, “Fano Enhancement of Plasmonic Raman Conversion,” article in preparation.
- [53] OriginLab Corporation, “Box Chart with Column Scatter Example.” [Online]. Available: <http://www.originlab.com/www/products/GraphGallery.aspx?GID=104>. [Accessed: 18-Jan-2017].